THESIS FOR THE DEGREE OF LICENTIATE OF ENGINEERING

EXPERIMENTAL EVALUATION OF A MICROWAVE TOMOGRAPHY SYSTEM FOR BREAST CANCER DETECTION

Tomas Rydholm

Cover:
Reconstruction of the permittivity of a cylindrical phantom with a smaller cylindrical inclusion.

To my grandfather
Arne Andersson
1923-2010

EXPERIMENTAL EVALUATION OF A MICROWAVE TOMOGRAPHY
SYSTEM FOR BREAST CANCER DETECTION
Tomas Rydholm
Department of Electrical Engineering
Chalmers University of Technology

Abstract

Microwave tomography is a potential candidate for future breast-cancer
screening or diagnosis. Contrary to x-rays, microwaves are non-ionizing and
therefore not a health risk by their own. The examination procedure would
also be more comfortable for the patient compared to conventional mam-
mography since no compression of the breast is needed.

The examination is performed by irradiating the breast with microwaves
from multiple directions. The collected data is then processed by an iterative
algorithm that reconstructs the permittivity and conductivity distribution
in the interrogated region. Ideally, tumors could be identified in these recon-
structed images due to their different properties compared to normal tissue.

In this thesis, a prototype system for microwave tomographic imaging
is experimentally evaluated. The system consists of 16 monopole antennas
and utilize a mixture of water and glycerin as coupling liquid. As a tool
for the assessment, two phantoms have been studied. One is a simplistic
phantom consisting of a cylinder in which smaller cylindrical inclusions can
be inserted. The other is a 3D printed structure made to resemble a human
breast geometrically. This particular phantom consists of two shells, repre-
senting the different tissues of the breast. The system is found to produce
well reconstructed images of both the interrogated phantoms. However, the
interior geometry of the 3D printed phantom was more challenging.

Furthermore, two different reconstruction algorithms are tested. The
first is a Gauss-Newton based FEM algorithm and the second is a gradient-
descent based FDTD method. Both of the studied algorithms proved to yield
good reconstructions.

Keywords: breast cancer, microwave imaging, phantom, tomography

Publications

This thesis is based on the following publications:

[A] **A First Evaluation of the Realistic Supelec-Breast Phantom**
T. Rydholm, A. Fhager, M. Persson, P. M. Meaney
IEEE J. Electromagn. RF Microw. Med. Biol. **1**, pp. 59–65, 2017.

[B] **Comparing a Time-Domain and Frequency-Domain Based Algorithm in Microwave Tomography**
T. Rydholm, A. Fhager, M. Persson, P. M. Meaney
12th European Conference on Antennas and Propagation (EuCAP), London, UK, 2018.

[C] **Effects of the Plastic of the Realistic GeePS-L2S Breast Phantom**
T. Rydholm, A. Fhager, M. Persson, S. D. Geimer, P. M. Meaney
Diagnostics **8**, 61, 2018.

Other publications by the author that are related to but not included in the thesis:

- **Microwave Tomographic Image Improvement by Fitting to a Cole-Cole Relaxation Model**
  T. Rydholm, A. Fhager, M. Persson, P. M. Meaney
  In Procceedings of the 11th European Conference on Antennas and Propagation (EuCAP), Paris, France, 2018.

- **Conformal mesh and two-step tomographic imaging of the Supelec breast phantom**
  P. M. Meaney, T. Rydholm, A. Fhager, M. Persson, N. Joachimowicz, C. Conessa, B Duchêne
  2016 IEEE Conference on Antenna Measurements Applications (CAMA), Syracuse, NY, USA, 2018.

- **Dielectric Probe**
  H. Brisby, P. M. Meaney, T. Rydholm, R. Augustine
  Patent Application No. 1850654-3 - Sweden, May 31, 2018.

- **Visualization of the Effects of Multipath Signals in Complementary Imaging and Dielectric Probing Scenarios**
  P. M. Meaney, T. Rydholm, S. D. Geimer, K. D. Paulsen
  2018 IEEE Conference on Antenna Measurements Applications (CAMA), Västerås, Sweden, 2018.

- **A Transmission-Based Dielectric Property Probe for Clinical Applications**
  P. M. Meaney, T. Rydholm, H. Brisby
  Sensors (submitted).

Other publications by the author not related to the thesis:

- **Towards more thermally stable Li-ion battery electrolytes with salts and solvents sharing nitrile functionality**
  M. Kerner, D. H. Lim, S. Jeschke, T. Rydholm, J. H. Ahn, J. Scheers,
  J. Power Sources **332**, pp. 204-212, 2016.

Acknowledgments

Writing a thesis and summarizing three years of work in a matter of pages is not an easy task. Still, writing an acknowledgement is certainly not any easier. There are far to many people I'd like to express my thanks to and I hope that I haven't forgotten any of you.

First, I'd like to thank everyone of my colleagues in the Biomedical Electromagnetics group for these three years we've worked together. My examiner and main supervisor Paul Meaney, my co-supervisors Andreas Fhager and Mikael Persson, and all the rest of the group: Morteza Aram, Stefan Candefjord, Hana Dobsicek Trefna, Samar Hosseinzadegan, Shantanu Padhi, Pegah Takook, Massimiliano "Max" Zanoli and Xuezhi Zeng.

To all my friends and "lunch buddies" from the Antenna Systems group: Navid Amani, Carlo Bencivenni, Wan-Chun Liao, Jinlin Liu, Sadegh Mansouri Moghaddam, Aidin Razavi, Madeleine Schilliger Kildal, Parastoo Taghikhani, and Abbas Vosoogh.

I would especially like to thank Måns Larsson, Johan Nohlert , Carl Toft, and Johan Winges for all our intriguing, helpful and interesting discussions on electromagnetic field theory, software defined radios, and computational methods; Helena Brisby, Lars Ekström, and Malin Erlandsson at Sahlgrenska University Hospital for our collaborations; and Ann-Christine Lindbom for all her administrative help.

To all my friends from Chalmers, high school, and elsewhere. I don't dare to name you in this list because I would surely forget someone who deserves my gratitude. You all know who you are anyway. Thanks for everything and always being there when I need you.

Finally, thanks to my family Bengt, May-Britt, Jonas, and Melinda for all the support and encouragement you've shown and for enduring my constant nagging about nerdy subjects all these years. I'd also like to thank my grandfather Arne for igniting my spark of curiosity and inspiring me to study physics and mathematics that eventually lead to this thesis.

<div align="right">Tomas Rydholm, Göteborg 2018</div>

x

Contents

Part I

Introduction

Chapter 1

Background

Breast cancer is one of the most common kinds of cancer among women. In Sweden alone, 35 268 women were diagnosed with the disease and 4 178 died from it during the six years period 2004–2009 [1]. That corresponds to roughly 16 new cases and two deaths each day among a population of just over nine million [2]. Early detection is a key aspect in putting in effective treatment and reducing mortality. If the tumor is detected at an early stage where it is confined to a local region around its origin, the five-year survival rate is as high as 99%. If, on the other hand, the cancer is not diagnosed until metastases have started to form, the corresponding survival rate decreases to 27% [3]. Novel technologies could increase the chances to early distinguish malign tumors from benign lesions and normal tissue.

1.1 Breast-cancer screening today

Breast imaging can be divided into three categories: screening, diagnosis, and therapy monitoring. Screening refers to routine scans of patients who do not necessarily show any signs of cancer. This is done in order to ensure an early detection of the cancer. If suspicious abnormalities are detected during screening or if the patient show signs of cancer, the next step is diagnosis. This can include further scans or biopsies. A patient who has been diagnosed with cancer is monitored through further scans during the treatment process in order to study the development and make sure that the cancer is suppressed.

The gold standard for breast cancer screening is mammography. It is an x-ray based imaging technique where projection images are taken of the breast in the craniocaudal and mediolateral oblique directions. This demands that the breast is compressed to even out the thickness, which the patient often finds uncomfortable or even painful. Mammography, although being an effective way of detecting potential cancers, has had some imperfections. A study by Säbel and Aichinger showed that 5–15% of all breast cancers

go undetected from mammography and that only 10–50% of all biopsies conducted based on mammographic screenings were necessary [4]. It also has a drawback in that tumors can be difficult to distinguish from ordinary glands, which is especially evident in denser breasts.

The most effective way of diagnosing breast cancer is through biopsy but a biopsy can be performed in different ways [5]. Tissue or fluids from the suspicious region is extracted and studied under a microscope. If the lump is likely to be filled with liquid, a fine-needle aspiration (FNA) is performed to extract the liquid. If the lump is not filled with liquid, tissue has to be extracted. This can be done via core-needle biopsy (CNB) for small samples, or a surgical biopsy for larger samples. The former of these utilizes a hollow needle of larger diameter than FNA. In the latter, the tumor or parts thereof are removed using a scalpel, typically together with some healthy tissue.

Monitoring can be done through different imaging techniques to see whether the cancer is responding to treatment and hence shrinking or not. Examples of these techniques include computerized tomography (CT or CAT) [6], magnetic resonance imaging (MRI) [7], and to some extent positron emission tomography (PET) [8]. These techniques will be described further in Chapter 1.2.

1.1.1   Anatomy of a female human breast

A human breast can roughly be divided into two tissue types: adipose and fibroglandular tissue. The adipose tissue consists mostly of fat. The fibroglandular tissue is constituted of glands and connective tissue. A visual description of the anatomy is presented in Figure 1.1.

Breasts are typically medically categorized depending on their fibroglandular density according to the Breast Imaging Reporting and Data System (BI-RADS). There are four categories used in BI-RADS: fatty, scattered, heterogeneously dense and extremely dense breasts. Fatty breasts consist mainly of adipose tissue. Scattered breasts are properly named so due to the scattered regions of fibroglandular tissue. In heterogeneously dense breasts, fibroglandular tissue constitutes the major part of the breast, and in extremely dense breast, there is almost no adipose tissue. Mammograms of breasts belonging to the four different categories are presented in Figure 1.2.

The breast density is important when searching for tumors. For traditional mammograms, tumors can be hard to locate in dense breasts due to their apparent similarities to glands. Hence, there exists a need to find alternatives to mammography that are both safe, comfortable, and have the ability to distinguish tumors also in denser breasts.
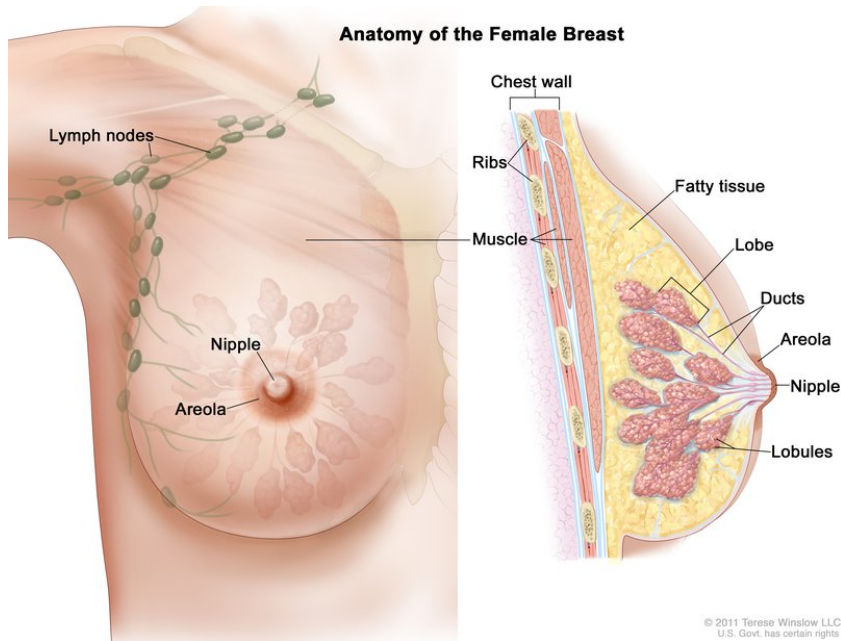
Figure 1.1: The anatomy of a female breast depicting the fatty (adipose) tissue and the glandular lobes. For the National Cancer Institute © (2011) Terese Winslow LLC, U.S. Govt. has certain rights. Used with permission.

1.2 Possible alternatives today

The disadvantages of mammography makes it desirable to find alternative ways of detecting breast cancer. Although there are other imaging techniques that theoretically could be used instead of mammography, they all have disadvantages of their own.

CT scanners are sometimes used when the patient has been diagnosed with a large cancer and the radiologist wants to determine if it has spread into the chest wall [6]. The patient is illuminated by x-rays from different angles via a toroidal system surrounding the body. The scan is processed to reconstruct imaged slices of the patient. There is ongoing research on minimizing the system to just image the breast, which could be a potential future candidate for breast cancer screening.

MRI scanners utilize strong magnetic fields instead of x-rays to find the distribution of polar molecules [7]. MRI is typically used in cases where the woman has already been diagnosed with cancer and further studies are wanted, e.g. the size of the tumor or whether the cancer has spread to the other breast. It is sometimes used as a screening tool in connection to mammography but is not recommended as a stand alone screening tool since it can miss certain tumors that a mammogram would have revealed. It has also a high chance for false positive findings and is quite expensive in
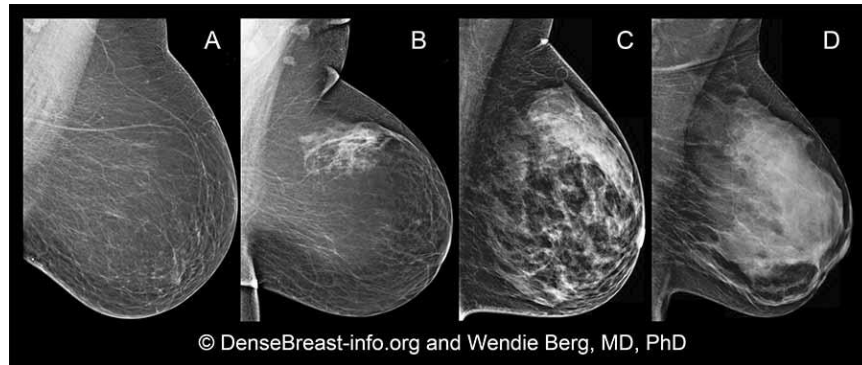
Figure 1.2: Mammograms depicting (A) fatty, (B) scattered, (C) heterogeneously dense, and (D) extremely dense breasts. © DenseBreast-info.org and Wendie Berg, MD, PhD. Used with permission.

comparison. Furthermore, the need of a contrast agent (typically gadolinium based) means that there are health risks for the patient [9].

In a PET scanner, the patient is injected with a radioactive sugar substance [8]. Due to the higher energy consumption of tumor cells, the sugar molecules are absorbed primarily by the tumors. As the radioactive substance decays, the PET scanner registers the origin of the radioactive bursts and forms an image depicting the cancerous regions. Although PET scanners are used to further study patients already diagnosed with cancer, it is not used as a screening tool due to high costs and low sensitivity for small tumors.

Ultrasound is a common diagnosis tool when an abnormality has been found and the radiologist wants to interrogate it further [10]. High-pitch sound pulses (outside the spectrum of human hearing) are sent through the breast and are deflected by the different breast tissues. The echoes are recorded and analyzed to reconstruct an image (sonogram) of the breast interior. Although being able to distinguish between cancerous tumors and harmless cysts, ultrasound is only helpful if the lump is big enough to easily be felt. It therefore falls short when it comes to be used as a screening tool.

Tomosynthesis is a new technique found at research level and at a limited number of hospitals [11]. It can be compared to regular mammography in that the breast is positioned between two glass plates and irradiated by x-rays. The advantage of tomosynthesis is that just a small pressure is applied to hold the breast steady without compressing it. Numerous x-ray images are then taken from different directions to form a 3D image of the breast.

At the moment, there is thus no real alternative to mammography when it comes to breast-cancer screening. New and novel techniques are needed in order to find a true alternative to x-ray mammography. A possible way could be to use microwave based systems.

1.3 Microwave imaging

Microwave based imaging has been of interest for the last few decades. The interest comes from the fact that healthy and cancerous tissue respond differently to electrical fields in the microwave part of the spectrum. Electromagnetics is the basis of many medical technologies. Electrocardiography (ECG), electroencephalography (EEG), and magnetoencephalography (MEG) have all reached clinical use for diagnosis and monitoring. Microwave based imaging has not reached that far yet but has matured to the level of clinical studies.

Microwave imaging could be a competing technique or a supplement to mammography that is both non-invasive, safe (the radiation is not ionizing), and comfortable. Although research within the field has been conducted for decades, microwave tomography is still in the stage of development. A major reason has been inadequate computational power, which today is no longer a problem [12]. These advantages makes it an interesting candidate both as a tool for screening and also for monitoring during the treatment.

Apart from breast cancer screening, microwave imaging has potential applications in a variety of fields. Among the medical applications there are research conducted in brain imaging [13–15], cardiac imaging [16], and bone density measurements [17]. Other fields include e.g. surveillance [18].

The idea to use microwaves for medical imagery can be dated back at least to 1979 when Larsen and Jacobi imaged a canine kidney *ex vitro* [19]. During the 1980's, more early microwave tomographic systems for medical applications were presented [20, 21]. Many of the first systems used linear reconstruction algorithms such as the Born approximation, which unfortunately showed problems when it comes to biological tissue due to high contrasts [22]. Later systems for medical applications have therefore moved on to more computationally heavy, non-linear reconstruction algorithms. As computers became more powerful, interest rose for the medical applications and breast cancer imaging became a hot topic around the millennial shift.

Today, several groups have come far in their development of microwave-imaging systems of which some have matured to the state of clinical studies. These systems are based on different principles: tomography (or inverse scattering), radar, and holography. These systems will further be discussed in Chapters 1.3.2 and 1.3.3.

1.3.1 A brief introduction to Microwave tomography

Tomographic methods differ from projection imaging techniques such as mammography in that the image is not directly created by the transmitted radiation. The target is instead illuminated from multiple angles and the collected data is used to reconstruct a cross-sectional image of the object and is thus more computationally heavy than projection-imaging techniques.
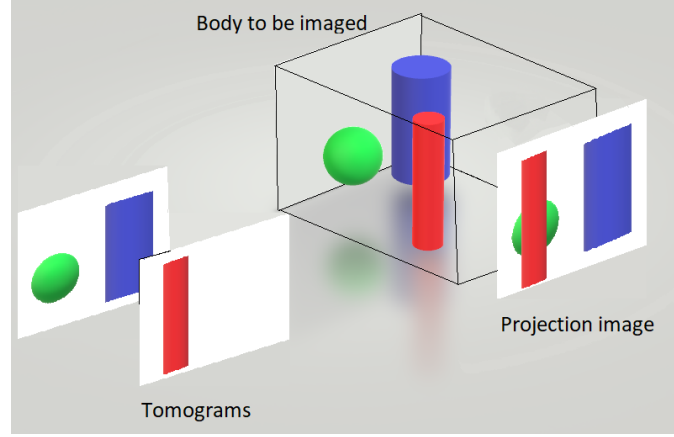
Figure 1.3: Illustration of the difference between a tomogram and a projection image. The two tomograms depict the contents of two distinct imaging planes whereas the projection image captures all of the present bodies.

Tomographic methods may thus capture distributions along the direction of propagation that projection imaging may not. This is illustrated in Figure 1.3. In the figure, three bodies are present in the imaging region. The shown projection image captures all present bodies, but it is not possible to tell their relative depths. The two tomograms, on the other hand, only depicts the contents of two particular imaging planes.

Microwave tomography belongs to a larger group of imaging techniques based on inverse scattering problems. The word "tomography" comes from the Ancient greek "τόμος" (tomos) meaning "slice" and "γράφω" (grapho) meaning "to write" and thus reflects how the method images two-dimensional cross sections of the target. Some systems are built to reconstruct a three-dimensional image, after the same principles as the two-dimensional tomographic systems. Occasionally, these are also referred to as tomographic systems although "inverse scattering imaging systems" would be a more correct definition. For the sake of simplicity and the fact that they operate under exactly the same principles as their two-dimensional counterparts, these three-dimensional imaging systems will also be referred to as tomographic systems throughout this thesis.

1.3.2 Microwave-tomography systems under development

This thesis revolves around an imaging system built after the same principles as the clinical one developed at Dartmouth college [23]. The system is based on 16 circularly arranged monopole antennas and utilizes liquid immersion medium. It will further be explained in Chapter 2.2.

Apart from the Dartmouth system, prototype tomographic systems for 2D- and 3D-reconstructions are under development at the University of

Manitoba [24, 25] and at Chalmers University of Technology [26]. Furthermore, simulation studies have extensively studied the tomographic methods [27, 28].

The group at the University of Manitoba has experimented with different realizations of air coupled systems surrounded by metallic walls. The motivation for the metallic walls was to eliminate the need for a lossy coupling medium and shielding the system from external sources [24]. One of the systems utilizes a faceted chamber meant to facilitate the numerical model further [25].

The first Chalmers system operated under similar principles as the Dartmouth one. The system is liquid coupled and utilizes monopole antennas as transceivers [26, 29]. This system has lately been set aside in favour of the one used in this project.

The importance of the work by Semenov *et al.* and EMTensor should also be emphasized. Although not focusing on the breast, they have had a leading role in microwave tomography [12, 30].

1.3.3 Other implementations of microwave imaging

Tomography is not the only microwave based diagnostic technique under development. Alternatives primarily include radar based technology but also holographic ones.

Whereas tomographic systems aim to reconstruct an image of the dielectric properties themselves, radar based systems try to map the location of microwave scatterers without determining their specific properties. It is thus a qualitative technique whereas tomography can be considered a quantitative technique. The technology is largely based on ground-penetrating radar and other previous military applications and has the advantage of a simpler signal processing compared to microwave tomography [31].

The radar-based system developed at University of Calgary [32], known as the Tissue Sensing Adaptive Radar (TSAR), is a liquid coupled system that utilizes a single antenna that is rotated around the breast, measuring at frequencies from 50 MHz to 15 GHz. A laser is directed towards the target and rotated around it together with the antenna to determine the imaging volume. The received signal is finally filtered in order to reduce the effects from reflections from the skin.

The MARIA system developed at University of Bristol is another radar based system [33]. Their prototypes have utilized 16, 31, and latest 60 slot antennas [33–35]. The antennas are here placed in a hemispherical shell surrounding the breast. It is a liquid coupled system where calibration (to subtract the scattering from the skin) is conducted by performing a second measurement where the antenna array has been rotated around its vertical axis.

Similarly, the McGill University system is based on a hemispherical shell

equipped with 16 antennas [36]. Ordinary ultrasound gel is used as coupling medium. This medium is used to fill air gaps between the radome and the breast. Also, due to its high conductivity, it attenuates multiply reflected signals.

The Wavelia system developed by MVG Industries is another radar based system worth mentioning [37]. It was recently installed at Galway University Hospital [37] and their first clinical studies are under preparation.

At McMaster University, a third related technology known as microwave holography has shown some success [38]. It is a technique inspired by optical holography. A target is illuminated by a coherent microwave signal. The scattered microwave signal is recorded much like an optical hologram but the reconstruction is conducted by applying Fourier transforms rather than by illuminating the recorded hologram [38]. These holographic approaches are already employed as a measure for detection of hidden weapons [39].

1.3.4   Clinical studies

The Dartmouth system has matured to the stage of clinical studies [40–43]. The group has demonstrated that tumor with a diameter larger than $1\,cm$ with statistical significance can be distinguished from benign lesions through their different properties [41]. Through their system, it has also been demonstrated how the average properties varies along with the breast density [42]. In a later study, the system is used to monitor the response of the cancer when treated through Neoadjuvant chemotherapy (NCT) [43]. The same study shows that the system is able to detect both the tumor and the thickening of the skin related to the cancer.

Other systems that have seen clinical studies include the ones developed at Bristol University, McGill University, and the University of Calgary. All these systems are radar based.

The Bristol group reported a clinical study on 86 subjects where the sensitivity compared to Ultrasound was $74\,\%$. This was comparable to the $78\,\%$ sensitivity of appurtenant mammograms.

The McGill system has been used in a clinical trial of monitoring [36]. 13 healthy patients were monitored over a range of two to eight months. The study concluded a small variability of the average permittivity over the monthly scans that, on the other hand, is insignificant to errors in the calculation.

The Calgary system (TSAR) was used to image eight patients [32]. The group reported a clear detection among the subjects with a distinct presence and location of a lesion. For the cases where the subjects had multiple lesions and gone through biopsy prior to examination were more difficult. Also, for the subjects that did not have cancer, false positives were detected by the system.

1.4 Electromagnetics and biological tissue

In this section, we will address the fundamentals of electromagnetics and the material properties governing the electric and magnetic fields. It is also discussed how these properties vary with the frequency of the applied fields (for certain materials) and what properties that have been reported for breast tissues.

1.4.1 Electromagnetic field theory

Electromagnetics are fundamentally determined by Maxwell's equation, which in their differential form are given by

$$\nabla \cdot \mathbf{E} = \frac{\rho}{\varepsilon_0} \tag{1.1}$$

$$\nabla \times \mathbf{E} = -\frac{\partial \mathbf{B}}{\partial t} \tag{1.2}$$

$$\nabla \times \mathbf{B} = \mu_0 \cdot \left(\mathbf{J} + \varepsilon_0 \frac{\partial \mathbf{E}}{\partial t} \right) \tag{1.3}$$

$$\nabla \cdot \mathbf{B} = 0 \tag{1.4}$$

where $\mathbf{E}$ is the electric field, $\mathbf{B}$ is the magnetic flux density[1], ε_0 is the free-space permittivity, μ_0 is the free-space permeability, ρ is the charge density (both free and bound charges), $\mathbf{J}$ is the current density (free and bound currents), and t is time. The current is related to the electric field through

$$\mathbf{J} = \sigma \mathbf{E}, \tag{1.5}$$

where σ is the electrical conductivity.

Furthermore, at a macroscopic level, two new fields can be defined that are independent of the bound charges and currents. These are usually denoted by $\mathbf{D}$ and $\mathbf{H}$ and are known as the electric displacement field and the magnetic field, respectively. For homogeneous, isotropic and non-dispersive media, the two fields are related to the fields above through the constitutive relations

$$\mathbf{D} = \varepsilon_r \varepsilon_0 \mathbf{E} \tag{1.6}$$

and

$$\mathbf{H} = \frac{1}{\mu_r \mu_0} \mathbf{B}, \tag{1.7}$$

where ε_r and μ_r are the relative permittivity and permeability of the material, respectively. Through this work, all materials of interest are non-magnetic and thus we will further on assume that $\mu_r = 1$.

---

[1]$\mathbf{B}$ is sometimes referred to as the magnetic field, even though that is the classical name for the field $\mathbf{H}$ defined in Equation (1.7).

The relative permittivity and the electrical conductivity of materials play a crucible role for electromagnetic propagation and thus for microwave imaging and will be revisited throughout this thesis. For the rest of the thesis, the electrical conductivity will always be referred to as just the conductivity.

1.4.2   Relaxation models

The dielectric properties of media are not constant but varying with respect to the frequency of an applied field. The permittivity and conductivity are often combined into a complex permittivity that then explains both the polarizability as well as electric losses of the material. Many models have been developed to explain the relationship between this complex permittivity and the frequency, of which the Debye relaxation model is one of the most common ones [44]. The complex relative permittivity ε^* is then given by

$$\varepsilon^*(\omega) = \varepsilon_\infty + \frac{\varepsilon_s - \varepsilon_\infty}{1 + \mathrm{j}\tau\omega}. \tag{1.8}$$

Here, ε_s and ε_∞ are the relative permittivities as the angular frequency ω approaches zero and infinity, respectively, and τ is the characteristic relaxation time. Equation (1.8) is derived for a set of ideal non-interacting dipoles and is a good model for e.g. water.

Not all media can be approximated as this and variations of the original Debye relaxation model have therefore been developed. First of all, it does not allow for a static current which exist if salt is added to the water. A DC-conductivity σ_s can then be added as

$$\varepsilon^*(\omega) = \varepsilon_\infty + \frac{\varepsilon_s - \varepsilon_\infty}{1 + \mathrm{j}\tau\omega} + \frac{\sigma_s}{\mathrm{j}\varepsilon_0\omega}. \tag{1.9}$$

Even more sophisticated models include multipole-relaxation models, where more than one relaxation term is included, and the Cole-Cole model, which accounts for a spectral spread of the relaxation peak [45]. The latter is given by

$$\varepsilon^*(\omega) = \varepsilon_\infty + \frac{\varepsilon_s - \varepsilon_\infty}{1 + (\mathrm{j}\tau\omega)^{(1-\alpha)}} + \frac{\sigma_s}{\mathrm{j}\varepsilon_0\omega}, \tag{1.10}$$

where α is the coefficient relating to the symmetric spread of the relaxation peak. Equation (1.10) gives a good description of e.g. glycerin and many kinds of biological tissues [46]. Although these more advanced relaxation models often give a better description of different media when studying a broad frequency range, the Debye model can often be a sufficient fit if the range is narrow enough.

Knowledge of the characteristics of different media are important when designing a phantom and tissue-mimicking media. Especially if the phantoms are to be used at multiple frequencies, their properties should correspond to the appropriate tissues at all of those frequencies.

1.4.3 Reported properties of breast tissue

The goal of microwave tomography is to map the permittivity and con-
ductivity distributions in the imaging region. This makes it an interesting
candidate for breast cancer screening since the different tissue types of the
breast as well as tumors have significantly different dielectric properties and
should thus be distinguishable in a microwave tomogram. This difference was
pointed out originally in 1926 by Fricke and Morse at 20 kHz [47]. Woodard &
White later reported similar results at higher frequencies [48]. Furthermore,
they showed the differences in properties between water, fat, and protein rich
content, which is essential for microwave imaging of breast tissue. Although
it is still debated what are the most representative values for the tissues, the
studies show that the contrast in dielectric properties is evident.

Numeral studies have been conducted to study the dielectric properties
of adipose and fibroglandular breast tissue and the resulting range of values
is fairly wide [49–54]. Apart from individual variations, this diversity can
partly be explained by issues existent with the open-ended coaxial cable
measurement technique [55–57]. It has also been pointed out that the *ex
vivo* measurements do not necessarily fully agree with the *in vivo* properties
[58, 59].

The dielectric properties of the adipose tissue have also proven to be
dependent of the radiographical density of the breast, due to the presence
of fibrogladular tissue in the otherwise fatty region [50, 53]. Lazebnik *et
al.* [50] and Martellosio *et al.* [53] each fitted a Cole-Cole model to their
measured data for three different breast densities. In Figure 1.4, several re-
ported studies of breast-tissue properties are presented. As for the different
densities reported by Lazebnik *et al.* and Martellosio *et al.*, the "low densi-
ties" have been grouped together with the adipose tissue of the other studies
and the "high densities" are grouped together with the fibrogladular tissue.
Similarly, the normal tissue studied by Cheng *et al.* [54] is stated to contain
both adipose and fibroglandular tissue but no ratios are given. From these
reports it is clear that variations between different studies are large and that
one cannot claim that one reported property model is the ground truth. Fur-
thermore, individual differences in breast density have a significant impact
on the dielectric properties of the tissue.
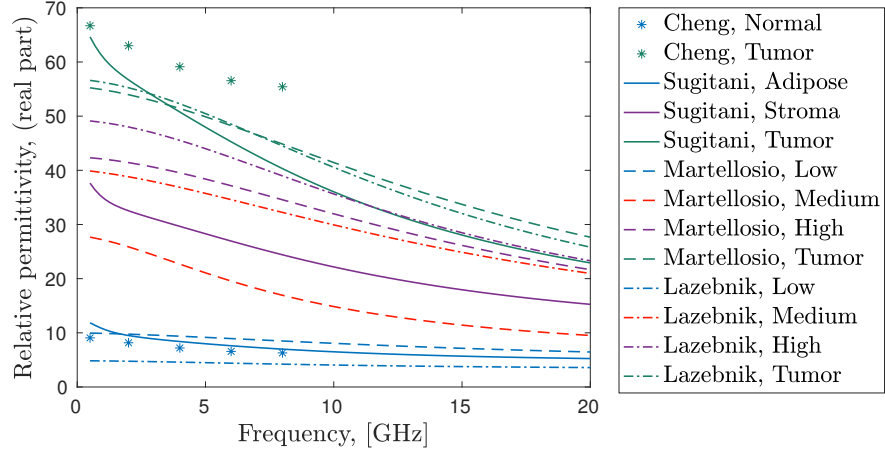
(a)
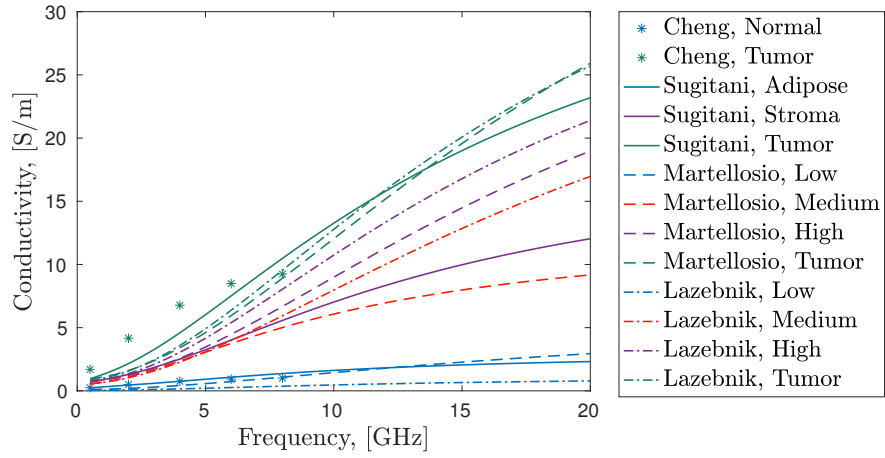
(b)

Figure 1.4: Dielectric properties as reported in several different studies, (a) relative permittivity and (b) conductivity. The tissues are grouped as: blue, adipose/low density; red, medium density; purple, high density; and green, tumor. Data retrieved from [50–54]. Reported standard deviations are omitted due to presentation reasons.

Chapter 2

Microwave tomography

Microwave tomography is an imaging method based on solving an electromagnetic inverse problem to calculate the spatial distribution of dielectric properties and quantitatively map the location of scatterers. In this chapter, the general principles of operation will be explained along with a description of the particular system used throughout this project.

2.1 Principles of operation

As was mentioned in Chapter 1.3.1, tomographic methods and projection methods differ from each other in how the image is formed. A projection image is just a shadow of the illuminated object whereas the tomographic approach makes it possible to map a distribution also in the signal's direction of propagation. In the case of microwave tomography, this illumination is performed by using antennas to irradiate the target with microwaves and the distribution being imaged is that of the dielectric properties ε and σ.

2.1.1 Hardware

A microwave-tomography system is thus based on a set of antennas. These antennas are placed such that they surround the region to be imaged. For a 2D-system, a suitable arrangement is a circle. The object to be imaged is placed inside this region. A schematic representation of this is given in Figure 2.1 The target is then illuminated from multiple directions. One at the time, each antenna transmits a signal while the other ones are used as receivers. The dielectric properties of the target will then impact the propagation of the fields which will manifest in the amplitude and phases of the signals received by the other antennas.

Although the dielectric properties of the target are unknown, the background (or coupling) medium should have known properties. A system can be air coupled, for which the properties of free-space ($\varepsilon = \varepsilon_0 = 8.85 \cdot$
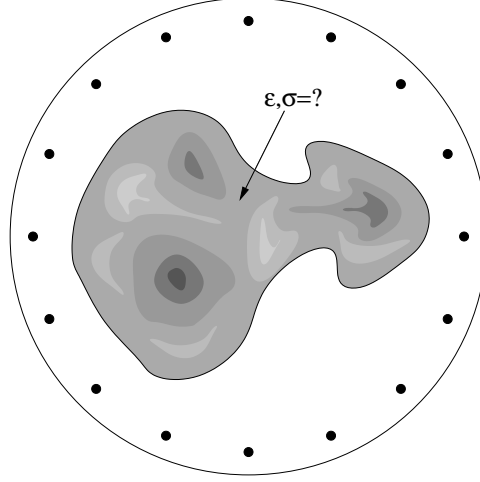
Figure 2.1: Schematic representation of an object of unknown permittivity and conductivity distributions placed in the imaging zone between the antennas.

10^{-12} F/m and $\sigma = 0$ S/m) can be used, but it is also common to use some sort of immersion liquid as coupling medium. The main reason for this is to lower the contrast in permittivity between background and target since a high contrast leads to high scattering from the surface of the target. By lowering this contrast, a larger part of the signals will penetrate into the target and instead scatter due to variations in the target's interior. A second reason to use a liquid coupling medium is the possibility to suppress e.g. unwanted reflections. This is achieved by using a conductive medium.

The recorded data is then processed by a numerical algorithm. Step by step, a computer tries to find a distribution of dielectric properties that yields the same results as the recorded data. Thus, an image of the interrogated target is reconstructed.

2.1.2   The numerical reconstruction

Electromagnetic numerical problems can be divided into two groups: forward and inverse problems. The first of these involves the computations of electromagnetic propagation through a known environment and is fairly easy to solve numerically. The goal of the latter is instead to calculate the properties of the environment from known features of the electromagnetic propagation. This is a much harder problem to solve and requires more sophisticated approaches. This is exactly the kind of problem microwave tomography is meant to solve.

In the numerical processing of the measured data, a solution to the inverse problem is typically found iteratively. In each iteration, a dielectric distribution is assumed and the *forward* problem using this distribution is solved. The solution is compared to the actual measured data and the dis-
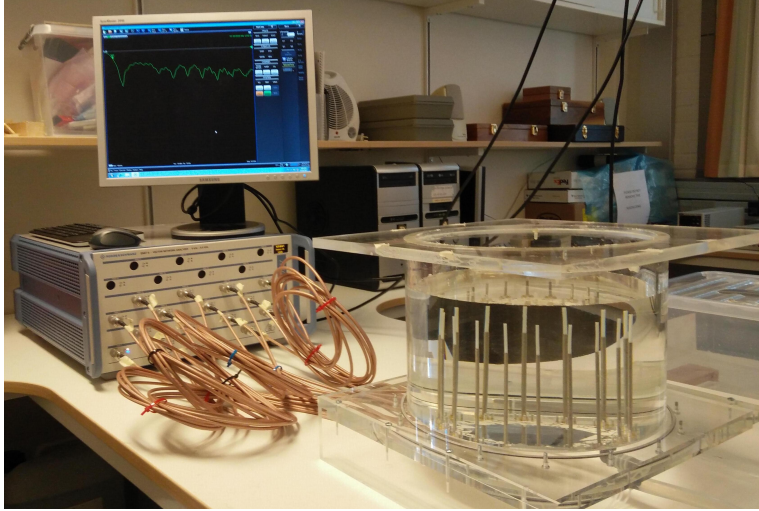
Figure 2.2: The prototype system used in this project. The 16 port VNA on the left is connected through coaxial cables to the antennas on the right. The antennas are immersed in a mixture of glycerin and water.

tribution is altered accordingly in order to decrease the difference between simulated and measured data step by step. After a certain number of iterations, the simulation converges to a solution sufficiently similar to that of the actual distribution.

2.2 The measurement system

The system utilized in this project is meant to image 2D slices of a human breast that is placed in the imaging region. A set of 16 antennas are arranged in a circle around the imaging region in order to illuminate the breast from all these directions. A liquid coupling medium is used to attenuate surface waves travelling along the antennas and to suppress unwanted effects from multi-path signals.

2.2.1 Detailed description of the system

The antennas used in this prototype are monopole antennas manufactured from rigid coaxial cables from which the outer conductor has been removed from the top three centimeters. These are placed on a circle of diameter 15.2 cm around the imaging area. The imaging plane roughly corresponds to the plane through the midpoint of these antennas. Of course, the imaging plane will in reality be some weighted average of the volume around this plane.

The system is depicted in Figure 2.2 The antennas are mounted inside a cylindrical tank of diameter 27.9 cm. This tank is then filled with a coupling
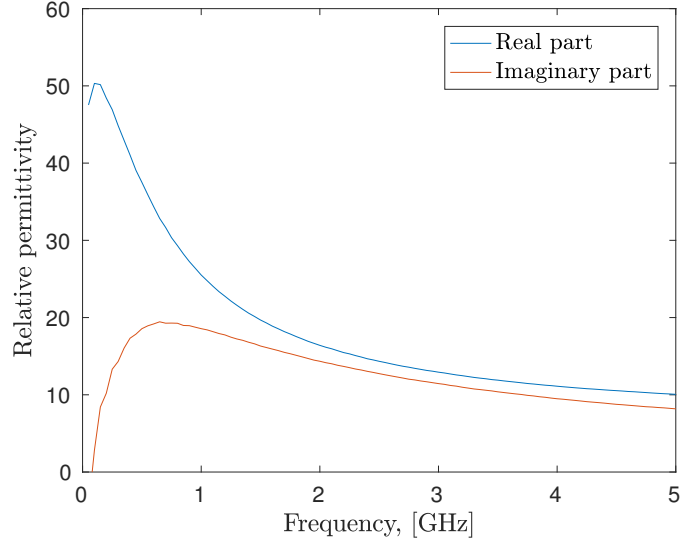
Figure 2.3: Real and imaginary parts of the relative permittivity of a mixture of 80% glycerin and 20% water.

medium based on glycerin and water, its surface typically around $3\,\text{cm}$ above the tips of the antennas. This coupling medium fills two functions. First, the liquid shows properties of conductive loss that effectively suppresses the surface waves and unwanted effects from multi-path signals. This means that the significant impact on the transmitted signals will come from the desired imaging plane. Second, the dielectric properties of the coupling liquid is closer to that of a human breast than air. This lower contrast in dielectric properties between the coupling liquid and the target means that reflections from the exterior of the target will be minimized. As coupling medium, a mixture of 80% glycerin and 20% water (volume percentage) has been used throughout this thesis. The dielectric properties of the mixture, as function of frequency, are presented in Figure 2.3.

A vector network analyzer (VNA) is used to operate the system. VNAs were originally designed to measure the reflections and transmissions of certain microwave devices by calculating the elements of their scattering matrices (S-matrices). Since these transmission coefficients are of interest for microwave imaging as well, the VNA makes a suitable device for the tomographic data acquisition as well. The elements of an S-matrix are given by

$$S_{ij} = \left. \frac{U_i^-}{U_j^+} \right|_{U_k^+=0,\ \forall k \neq j} \tag{2.1}$$

where S_{ij} is the i-row j-column element of the S-matrix, U_i^- is the outgoing voltage on port i of the antenna system, and U_j^+ is the incoming voltage on

port j [60]. These parameters are generally complex-valued to account for the phase differences between the outgoing and incoming signals.

A VNA has two or more ports that are connected to the antennas, either directly or through a switching matrix depending on the number of ports of the VNA and the number of antennas. The complete S-matrix is then recorded and used to reconstruct the image. In this prototype, the system is connected to a VNA of model Rohde & Schwarz ZNBT-8. This VNA has a dynamic range of 130 dB which allows for detection of weak signals, and a channel-to-channel isolation greater than 150 dB to minimize the cross talk between the channels. This particular device has 16 ports, eliminating the need for an external switching matrix.

2.2.2 Measurement procedure

During the measurement, each antenna consecutively transmits a signal at a predefined frequency or set of frequencies and the received signals at all antennas are recorded. This builds up the complete complex-valued S-matrix, although the reflection coefficients S_{ii} will not be used in the reconstructions. It is, however, necessary to calibrate the system, which is done by recording an identical measurement for just the homogeneous background, i.e. the coupling liquid. How the target affects the transmitted signals is found by studying the difference between these two data sets. The target will affect the signal both in terms of its amplitude and by delaying or advancing the propagation, i.e. affecting the phase of the recorded signal. The difference between these two data sets, in terms of phases and logarithmic amplitudes, are then used as input to the reconstruction algorithm.

2.3 Reconstruction algorithms

As was briefly mentioned above, inverse problems such as tomography demand more sophisticated methods than forward problems. For tomography in general, not restricting oneself to microwave tomography, the most common examples are iterative methods and methods based on transforms, e.g. the Radon transform [61]. Transform based methods generally yield more visual artifacts and iterative methods are thus often preferable. The solving of the inverse problem is combined with executions of the forward problem on a simulation domain that incrementally is altered to resemble the actual environment as iterations progress. Since microwave tomography is a subject for multiple scatterings, iterative methods are used whereas transform methods are found in e.g. CT.

In this section, we will take a closer look at two different reconstruction algorithms: a finite element method (FEM) based algorithm developed by Meaney *et al.* and a finite difference time domain (FDTD) based algorithm developed by Fhager *et al.* These algorithms were developed along their

respective groups' imaging systems. Of these two, the FEM algorithm thus constitutes the major part of the project but an initial comparison between the two algorithms has been performed as a basis for an upcoming bench-marking.

It should further be noticed that the distinction between FEM and FDTD is in the forward solver. The two reconstruction algorithms, however, also utilize different approaches to the reconstruction process as will be described below.

2.3.1 Finite element method

The algorithm developed by Meaney *et al.* is a Gauss-Newton based iterative FEM algorithm [62, 63]. The algorithm can be divided into two steps. The first 50 iterations incorporate a smoothed Levenberg-Marquardt method and the last 20 iterations incorporate a Tikhonov regularization with a Euclidean-distance penalty term [63].

The algorithm also utilizes a logarithmic transformation (log transform) of the field values that essentially describes the values in terms of phases and logarithmic amplitudes rather than their real and imaginary parts [64, 65]. The advantage of this is that information is retained as to which Reimann sheet the values belong to, which is lost if they are expressed in Cartesian form. Effectively, this means that the algorithm avoids converging to local minima which improves the image quality and obviates the need for *a priori* information.

The cost function (or penalty function) that is sought to be minimized is given by

$$f(k^2) = ||\Gamma^m - \Gamma^c(k^2)||^2 + ||\Phi^m - \Phi^c(k^2)||^2. \tag{2.2}$$

Here superscripts m and c refer to the measured and computed values, respectively, Γ refers to the logarithmic amplitudes, Φ refers to the phases, and k is the wavenumber.

Levenberg-Marquardt step

The cost function is first minimized through the Levenberg Marquardt method. This method is implemented as follows [63]

$$[J^{\mathrm{T}}J + \lambda I](\Delta k^2) = J^{\mathrm{T}}f(k^2). \tag{2.3}$$

Here, J is the Jacobian matrix, $J^{\mathrm{T}}J$ is an approximation of the Hessian matrix, λ is a damping coefficient, and $f(k^2)$ is the cost function given above. The value of λ can here be seen as a weighting between a Gauss-Newton and a gradient-descent part of the equation. The final k computed is then used as initial guess for the Tikhonov regularization.

Tikhonov step

The cost function is now altered by introducing an extra penalty term from the previous step [63].

$$f_T(k^2) = ||\Gamma^m - \Gamma^c(k^2)||^2 + ||\Phi^m - \Phi^c(k^2)||^2 + \gamma||k^2 - k_{int}^2||^2 \qquad (2.4)$$

Here, γ is an empirically determined regularization term and k_{int} is the intermediate wavenumber computed by the final Levenberg-Marquardt step. In practice, this alteration to the cost function means that the final solution should not be found to far away from the intermediate one.

It is worth noting that throughout this process, the dielectric properties have not been utilized *per se*. The reconstruction process has only computed the complex valued k^2 at each node in the numerical mesh. However, the relative permittivity and conductivity can be obtained from this through the relation

$$k^2 = \omega\mu_0\varepsilon_0\varepsilon_r + \mathrm{j}\omega\mu_0\sigma. \qquad (2.5)$$

2.3.2 Finite difference time domain

The algorithm developed by Fhager *et al.* is an iterative gradient-descent based FDTD algorithm [66, 67]. Much like the algorithm described above, the forward solution is computed in each iteration where the residuals between computed and actual measured data is used to adjust the computational domain. The computational domain is described by a Debye relaxation model and it is hence the coefficients of Equation (1.9) that are altered in each iteration [67].

The algorithm takes S-matrices measured at discrete frequencies as input, although the computation itself is done in the time domain. Numerically, a pulse is synthesized by applying an inverse Fourier transform to the collected data. This pulse based on measured data will here be denoted $\mathbf{E}_m^{meas}(\mathbf{R}_n, t)$, where $\mathbf{E}$ is the electric field, m denotes the m:th transmitter, *meas* indicates measured data, $\mathbf{R}_n$ marks the location of the n:th receiver and t is the time. For each iteration step, a numerical field will be calculated for the computational model of that particular iteration. This computed field will be denoted $\mathbf{E}_m^{comp}(\varepsilon, \sigma, \mathbf{R}_n, t)$, where *comp* indicates computed data, and the permittivity and conductivity distributions are given by ε and σ, respectively. For each iteration, the following cost functional is minimized.

$$F(\varepsilon, \sigma) = \int_0^T \sum_{m=1}^M \sum_{n=1}^N \left(|\mathbf{E}_m^{comp}(\varepsilon, \sigma, \mathbf{R}_n, t) - \mathbf{E}_m^{meas}(\mathbf{R}_n, t)|^2 \right) \mathrm{d}t \qquad (2.6)$$

Here T is the pulse duration time, M is the total number of transmitters, and N the total number of receivers.

Fhager *et al.* have further proven that their reconstructions can be improved by dividing the reconstruction into more than one step [68]. First,

a numerical pulse centered around a fairly low frequency is used for a few iterations. A low frequency means a large wavelength and consequently less details will be apparent in this intermediate image. On the other hand, it yields a better representation of the more large scale features. After a few iterations, the center frequency is stepped up. This process is repeated for higher and higher center frequencies. The result of this procedure is a more accurate reconstruction that avoids artefacts.

Chapter 3

Phantoms

Phantoms are models made to resemble organs or body parts both in terms of geometry and physical properties. They are an essential part of developing and evaluating a system and phantom studies bridges the gap between numerical and clinical studies. Phantoms also make it possible to perform studies on targets where the properties of the target is fully known, compared to actual biological tissue which can show significant variations among different individuals. In the case of breast-cancer diagnosis, phantom studies play an even larger role since there are no suitable animal counterparts to a human breast.

3.1 Tissue mimicking media

For microwave imaging, the dielectric properties are of interest. Thus, the phantom should have permittivity and conductivity distributions similar to those of a human breast. Many different kinds of media have been proposed as bases for suitable tissue mimicking materials. Important ones to mention are liquids such as Triton X-100 [69] and glycerin [70], and different gels such as agar [71]. The particular properties of interest are often obtained through different concentrations with water and salt. Gel based phantoms have the advantage of being solid but they degrade over time. Liquids on the other hand are in general more easily mixed but need some sort of vessel.

Other phantoms are made of solid materials. Some are meant to be used on their own whereas others are vessels for liquid phantom media. Materials designed for their dielectric properties are rubber-carbon mixtures and conducting plastics. There are also phantoms 3D-printed out of plastic. Of particular interest for this thesis is the GeePs-L2S phantom developed at the Supelec institute [69] which will be further discussed in Chapter 3.2.

Glycerin-water mixtures of different ratios have been the primary kind of phantom media in this project. A thorough study on the dielectric properties of glycerin-water mixtures as function of the constituent ratio was conducted

Tissue to mimic	Glycerin, %	Water, %
Tumor	55	45
Fibroglandular	72	28
Adipose	80	20
	84	16
	88	12
	97	3

Table 3.1: Content of mixtures used to mimic tumors, fibroglandular tissue and adipose tissue for different breast densities. For the adipose tissue, four different concentrations have been used.

over the frequency range $100\,\text{MHz}$–$25\,\text{GHz}$ by Meaney *et al.* [70].

Glycerin and water are miscible liquids that separately each have quite diverse dielectric properties. At $2\,\text{GHz}$, pure water was measured to have a relative permittivity 79 and a conductivity of $0.98\,\text{S/m}$, whereas glycerin at the same frequency was measured to have the relative permittivity 7.4 and the conductivity $0.46\,\text{S/m}$. The measurements have been conducted with dielectric probe (Agilent 85070 Performance Probe). By mixing these liquids, the dielectric properties of the mixture may be varied over a large range.

The glycerin-water mixtures mainly used through this project were originally developed by Meaney *et al.* to represent breasts of different densities, pure fibroglandular tissue, and tumors. The ratios between glycerin and water for these mixtures are presented in Table 3.1 and the measured dielectric properties are presented in Figure 3.1.

Although the dielectric properties of true breast tissue are still under considerable debate, as was seen in Figure 1.4, the use of glycerin-water mixtures allows for huge variability in the design of phantoms. They therefore enable rigorous tests of the imaging system over a wide frequency range.
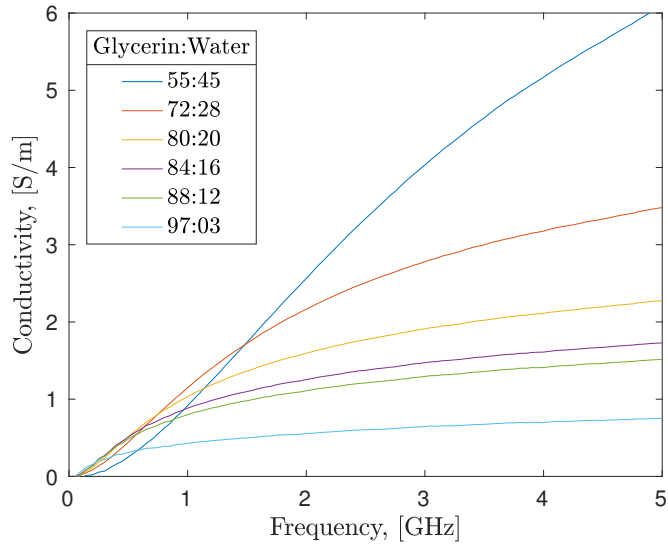
3.2   The GeePs-L2S phantom

At the Supelec institute in France, a geometrically realistic phantom has been developed [69]. It is a 3D-printed structure based on MR scans of an actual human breast. Its geometry thus captures the geometry of both the exterior as well as the interior very well. The phantom consists of two separate shells defining the exterior and interior geometry respectively. The two shells are shown in Figure 3.2. To emphasize the interior geometry, MR based images of 6 coronal planes of the phantom are depicted in Figure 3.3. The depicted planes are each separated by $1\,\text{cm}$ and their relative orientation are shown in Figure 3.4 showing a transversal cut of the phantom.

The phantom's two plastic shells correspond to the adipose and the fi-
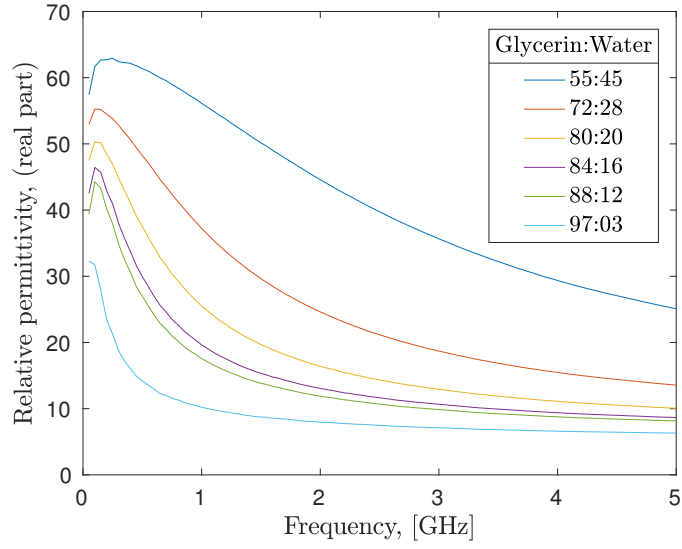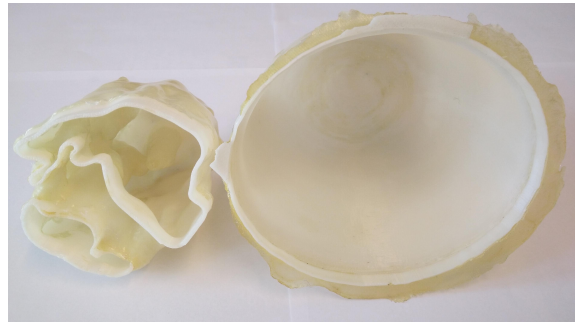
(a)

(b)

Figure 3.1: Dielectric properties of the used glycerin-water mixtures, (a) relative permittivity (real part), (b) conductivity.

(a)

(b)

Figure 3.2: The two shells of the GeePs-L2S phantom, (a) side view, (b) top view.

broglandular regions, respectively. The outer shell is around 2 mm thick and regularly shaped; the coronal cross sections can be approximated as ellipses. The inner chamber on the other hand has an irregular "wrinkled" shape. This means that the plastic ratio of each cross sectional plane is much higher than for the outer shell. Alternatively, it can be seen as having a larger effective thickness than the outer shell, although the thickness of the wall itself is roughly 2 mm just as in the previous case.

The phantom is made of the plastic Acrylonitrile butadiene styrene (ABS) which has a reported permittivity of 3 at 2.4 GHz [72]. Compared to the reported data of biological tissue, previously presented in Figure 1.4, this is significantly lower than many reported results, especially compared to the fibroglandular tissue. This, in combination with the high effective thickness could be a potential problem for imaging purposes.

The main rationale for developing the GeePs-L2S phantom is to have a common reference for benchmarking of imaging systems. The phantom has therefore been circulated around the world for different studies of both the phantom and different imaging systems via the COST Action TD1301 MiMED. However, only a few publications regarding this specific phantom have been released including the three papers that this thesis is based on.
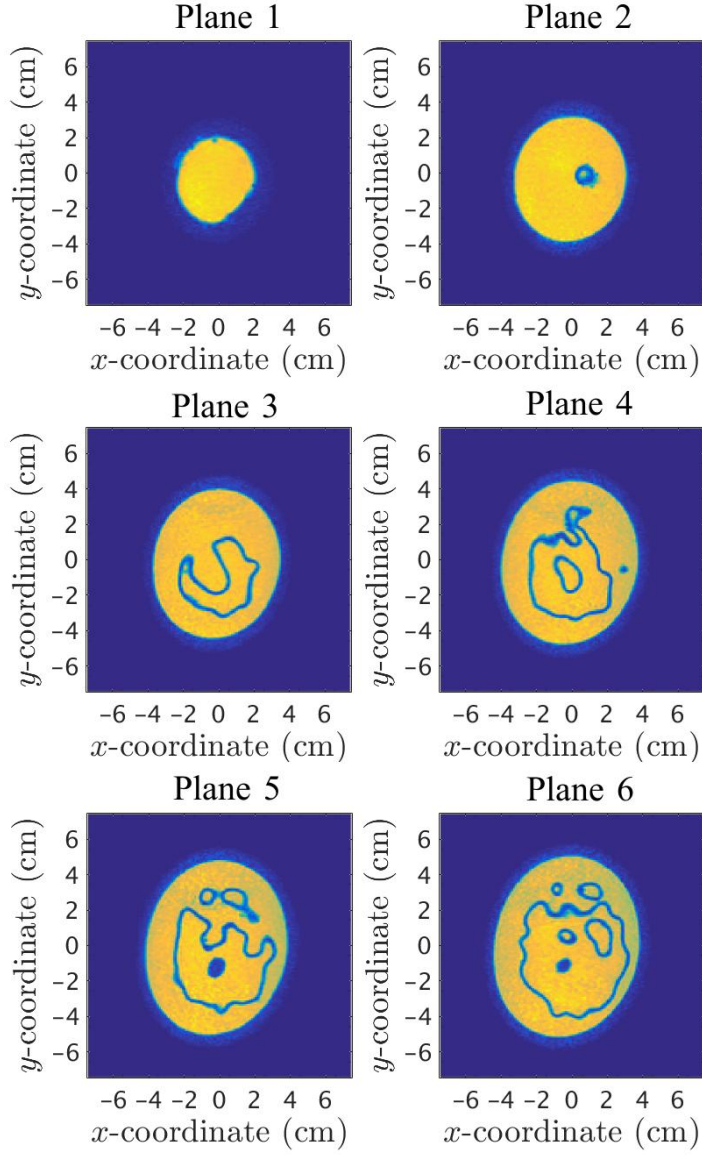
Figure 3.3: Coronal planes of the GeePs-L2S phantom. The planes are separated by 1 cm.
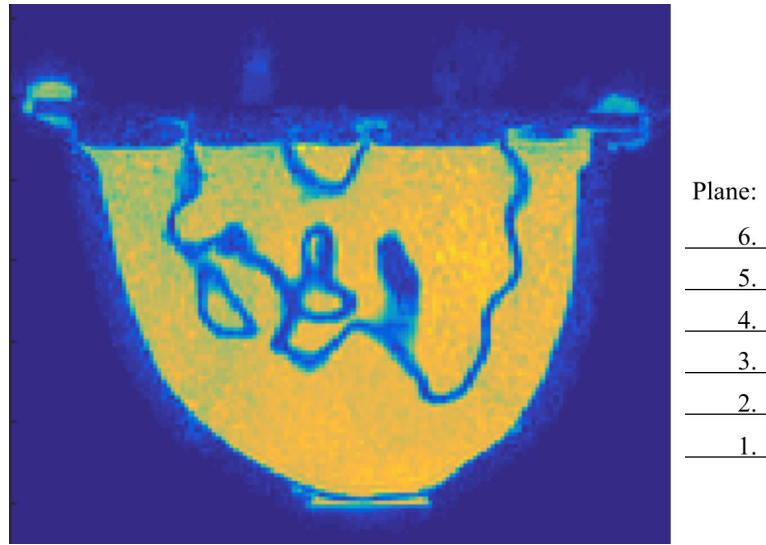
Figure 3.4: Transversal plane of the GeePs-L2S phantom. The planes presented in Figure 3.3 have been marked out.

The group at National Technical University of Athens has made an initial study using the phantom [73]. In this study, mixtures of distilled water, sugar, agar, and salt are used in different concentrations for adipose, fibroglandular, and tumor tissues. No images are produced but the group does detect that inclusion of a tumor has an impact on the S-parameters, both in amplitude and phase.

A second research group that has shown preliminary results is located at Politecnico di Torino [74–76]. Studies utilizing the phantom have been performed where pure water and Triton X-100 have been used [74, 75], as well as mixtures thereof [76]. Reconstructed images have been presented. However, they are very limited and only depict the "tumor inclusion" but no other features of the breast phantom.

It should also be mentioned that similar phantom structures have been developed at the University of Manitoba [77]. These phantoms are made to resemble different sizes and types of breasts.

3.3   Phantom experiments

During this project, primarily two phantoms have been studied. One is the GeePs-L2S phantom described above. The other is a more simplistic phantom based on a large cylinder and the possibility to introduce cylindrical inclusions. In this section, reconstructions of the two phantoms will be presented.

The system has shown capability of performing valid reconstructions at

Figure 3.5: The simplistic phantom used to study the robustness of the system. Here, the major cylinder is shown together with a cylindrical inclusion.

frequencies at least in the range $1.1 - 1.9\,\text{GHz}$. All measurements presented below were conducted with an output power of $0\,\text{dBm}$, an IF bandwidth of $10\,\text{Hz}$, and averaged over 10 measurements.

3.3.1 Simplistic phantom

In order to test the robustness of the system, a simplistic phantom was studied. The phantom, shown in Figure 3.5, was made of a thin cylindrical shell of plastic (polyethylene terephthalate: PET) with the possibility to insert smaller cylinders as inclusions. The major cylinder had a diameter of $105\,\text{mm}$ and the smaller ones ranged between 18 and $42\,\text{mm}$. The thicknesses of the cylinders were roughly $0.5\,\text{mm}$. The inclusions are typically used to represent either tumors or the fibroglandular zone whereas the major cylinder is filled with a mixture mimicking the properties of adipose tissue or a mix of the two tissue types corresponding to the different breast densities.

Below, reconstructed images of this simplistic phantom will be presented using the two reconstruction algorithms presented in Chapter 2.3. For this particular experimental case, a cylinder of diameter $42\,\text{mm}$ was used as an inclusion. This particular inclusion was chosen due to its similarity in size to the inner shell of the GeePs-L2s phantom. The orientation of the two cylinders is presented in Figure 3.6, which also depicts the ground truth values of the relative permittivity and conductivity as measured at $1.5\,\text{GHz}$.
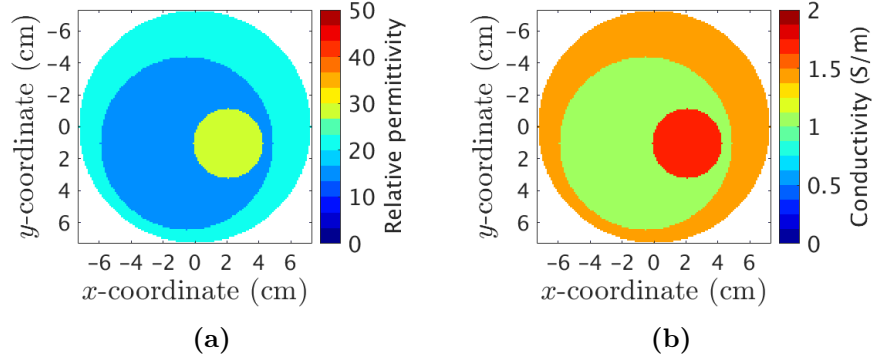
Figure 3.6: Phantom orientation and ground-truth values of the (a) permittivity and (b) conductivity at 1.5 GHz. The three circles (from outer to inner) represent the coupling bath, the main phantom, and the inclusion.

The center of the major cylinder has been displaced 5 mm to the left and 10 mm down from the center of the imaging region. The minor cylinder was then displaced 20 mm to the right from the center of the major one. The phantom was designed to represent a scattered breast, meaning that an 88:12 glycerin-water mixture was used in the outer cylinder. For the inner one, a 72:28 solution was used to mimic the fibroglandular region.
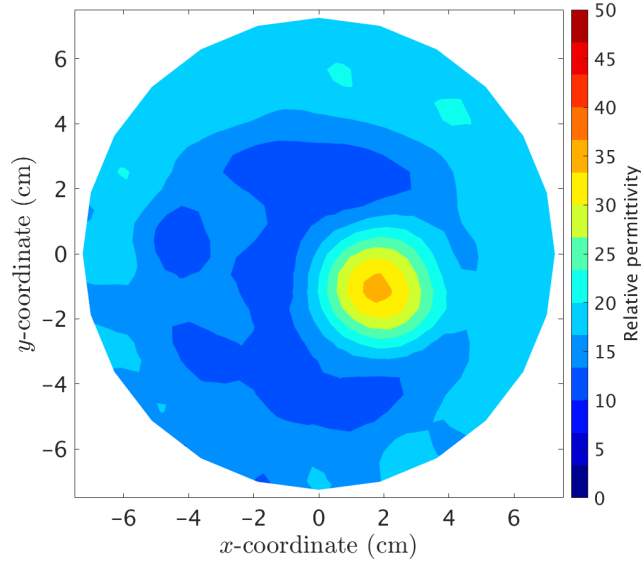
FEM reconstructions

The FEM algorithm utilizes measured data from one specific frequency. In the case studied here, the frequency 1.5 GHz is used. The reconstructed image is presented in Figure 3.7. Compared to the ground truth presented above, it is possible to see that the phantom is well reconstructed both in shape and properties, especially for the permittivity. The conductivity of the inclusion is a bit low but clearly distinguishable. For the permittivity it can be seen that the properties of the inclusion is somewhat overshot in its center. This is a remnant of the smoothing effects of the reconstruction algorithm.

FDTD reconstructions

For the FDTD reconstructions, a much larger set of frequency data had to be used. The forward solver was set to utilize a pulse centered around 1.5 GHz with an FWHM bandwidth of 0.6 GHz. Hence, measurements at 401 equally spaced frequency points over the same interval was used as input data. 20 iterations were performed to obtain the image.

For each node in the reconstruction mesh, a Debye-relaxation model is fitted. The interpolated data for the studied frequency (1.5 GHz) is presented in Figure 3.8. Also for this algorithm, the reconstructed image is a

(a)
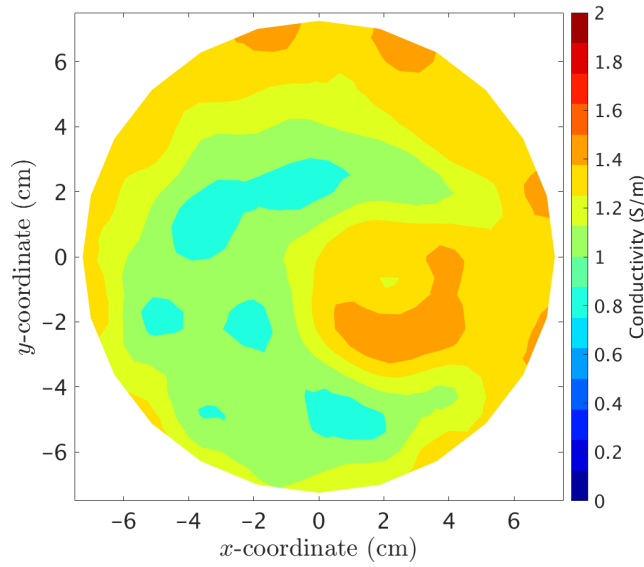
(b)

Figure 3.7: Reconstructions of the (a) permittivity and (b) conductivity for the cylindrical phantom at 1.5 GHz.
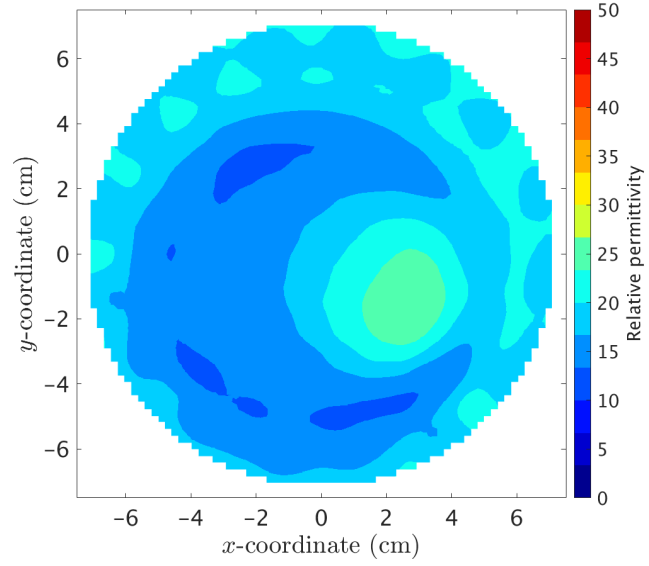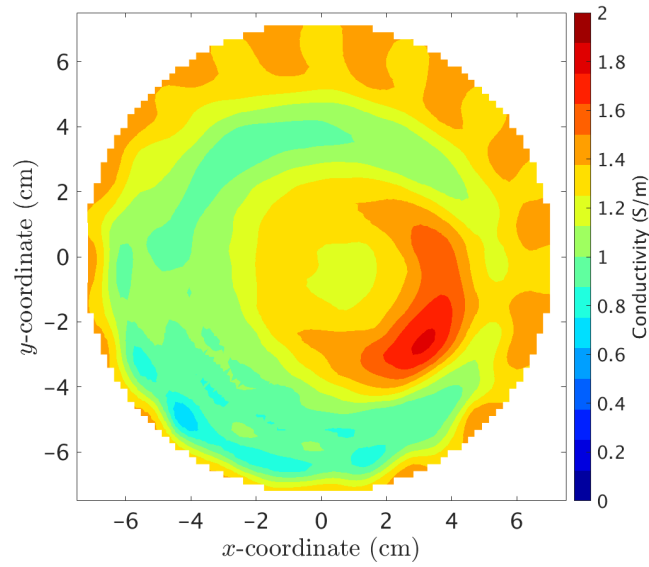
(a)

(b)

Figure 3.8: Reconstructions of the (a) permittivity and (b) conductivity for the cylindrical phantom at $1.5\,\mathrm{GHz}$.

good representation of the actual phantom. The general shapes are clearly defined and the properties are comparable to ground truth. However, the permittivity of the inclusion is now slightly undershot and in the conductivity image, the inclusion is deformed showing a hollow structure. This is a known issue of the algorithm that could be improved by optimization of the reconstruction settings.

3.3.2 Reconstructions of the GeePs-L2S phantom

Below follows a few examples of reconstructed images of the GeePs-L2S phantom using the system described in this thesis and the FEM algorithm described in Chapter 2.3. In Figure 3.9 the outer shell is filled with an 88:12 glycerin-water mixture representing the adipose tissue and the inner shell is filled with a 72:28 solution representing the fibroglandular tissue. Three planes of the phantom are depicted to emphasize its variable cross section. The sizes of the cross sections and the interior geometry should be compared to the MRIs presented previously in Figure 3.3. This particular measurement was conducted at 1.5 GHz. From these images, the varying cross sectional area of the phantom is clearly retrieved and can be compared to the MRI presented in Figure 3.3 above.

In Figure 3.10, images of the fifth plane (as denoted in Figure 3.4) are presented at the three different frequencies 1.1 GHz, 1.5 GHz, and 1.9 GHz. The same mixtures as above are used. The exterior shape of the phantom is clearly depicted at all these frequencies and the interior is present but not as well reconstructed as the exterior.

As can be seen from these sets of reconstructions, the system is capable of imaging the phantom within the studied frequency interval. However, although the exterior shape of the phantom is well reconstructed, there are problems to reconstruct its interior features. This should be compared to the reconstructions of the simplistic phantom presented above for which the interior was clearly depicted when the same tissue mimicking liquids were used.
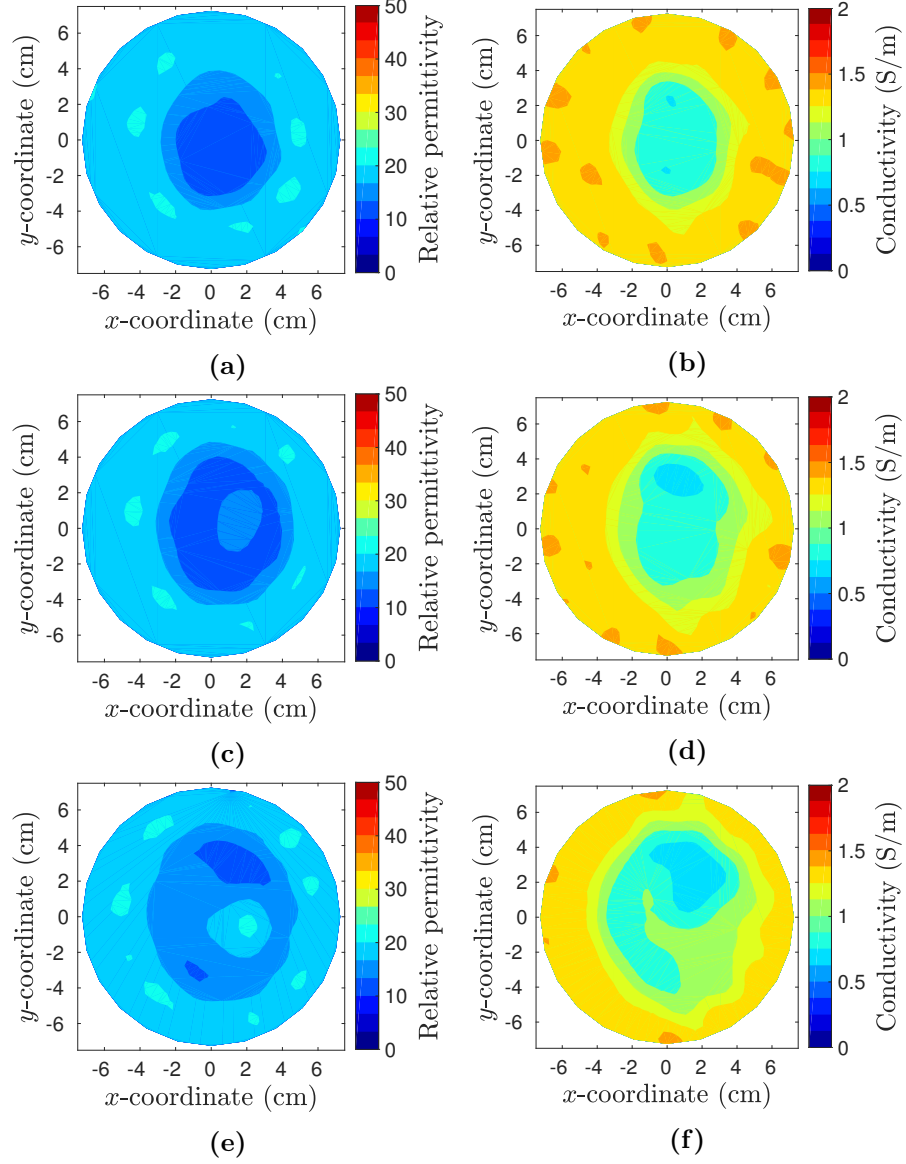
Figure 3.9: Reconstructions of the GeePs-L2S phantom at 1.5 GHz. First column (a, c, e) shows the permittivity and the second (b, d, f) shows the conductivity. Three planes are depicted as denoted in Figures 3.4 and 3.3: (a, b), Plane 1; (c, d), Plane 3; and (e, f), Plane 5.
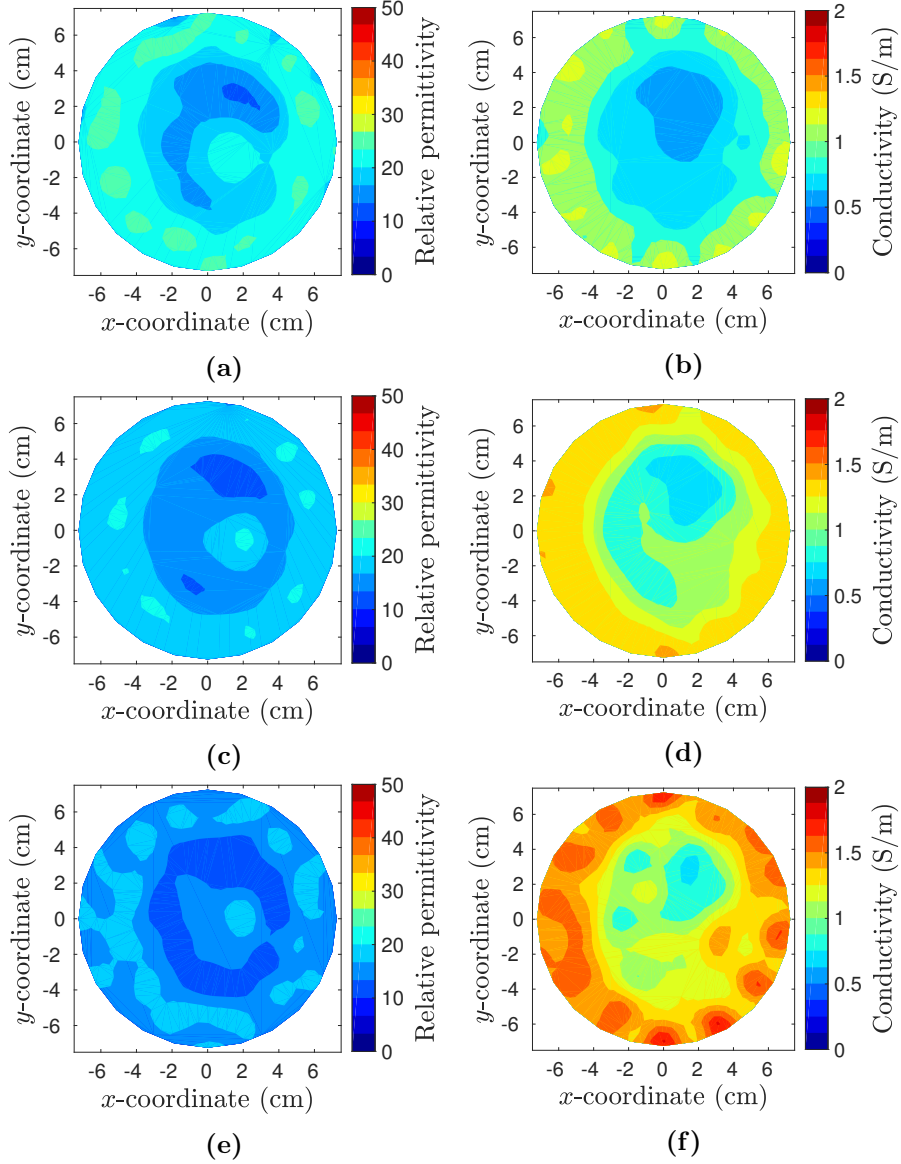
Figure 3.10: Reconstructions of the fifth plane of the GeePs-L2S phantom at three different frequencies. First column (a, c, e) shows the permittivity and the second (b, d, f) shows the conductivity. The reconstructions are performed at three different frequencies: (a, b), 1.1 GHz; (c, d), 1.5 GHz; and (e, f), 1.9 GHz.

Chapter 4

Summary of papers

In this chapter, the three papers that this thesis is based on will be summarized. The figures are not reproduced here and the reader is referred to the appended papers at the end of the thesis.

4.1 Paper A

This paper presents our initial study of the GeePs-L2S phantom. However, in the paper the phantom is referred to as the "Supelec phantom". The hardware described in Chapter 2.2.1 of this thesis was used together with the FEM-based algorithm described in Chapter 2.3.1. This was the first published study using this particular prototype system. The paper therefore starts with a verification of the system by studying a simplistic cylindrical phantom of similar cross-section area and properties as the GeePs-L2S phantom.

It is shown that the system can reproduce this simplistic phantom very well. The cylindrical phantom contained an inclusion to be compared to the inner shell of the GeePs-L2S phantom. These two cylinders were filled with the same water-glycerin mixtures as the GeePs-L2S phantom and measured over the interval 1.1 – 1.9 GHz. Images of this phantom at the two most extreme frequencies (1.1 and 1.9 GHz) are presented to show the capability of the system. The phantom and its inclusion appear clearly in the permittivity images and the locations of the reconstructed cylinders are perfectly comparable to the true locations, which have been marked out as red circles in the images for comparison. Also in the conductivity images, the phantom is reconstructed well, although not as well as in the permittivity images.

Following this verification of the imaging system, the results of the GeePs-L2S phantom are presented. First, six different planes, each separated by one centimeter, are imaged at 1.5 GHz. It is clearly seen how the cross sectional area is smaller close to the nipple and larger close to the chest wall. This is followed with a series of images of the fifth plane, counting from the nipple, at five equidistantly separated frequencies between 1.1 and 1.9 GHz.

Although the exterior shape of the phantom is clear and imaged well, the interior part is not. In several images it is possible to see traces of an inner structure but in most cases it is not visible. We therefore present the hypothesis that the thick plastic of the inner shell makes it hard to image via this procedure. To further investigate this hypothesis, the study was later continued in Paper C below.

4.2   Paper B

This paper presents an initial comparison of the two algorithms presented in Chapter 2.3 of the thesis. A numerical environment simulating the experiments of the cylindrical phantom from Paper A was designed and S-parameters were calculated by solving the forward problem.

Table 1, Figure 1, and Figure 2 present Debye functions that have been fitted to probed dielectric data of the three liquids used in the previous paper in the frequency range $0.5 - 2.0\,\mathrm{GHz}$. This fitted data was then used to describe the numerical model to the FDTD algorithm.

For the FEM code, a mesh of 3903 finite elements were used for the forward solver to generate S-parameters, whereas a mesh of 559 finite elements were used for reconstruction. This was done at the frequency $1.5\,\mathrm{GHz}$.

The forward solver dedicated to this code was used to generate S-parameters between $3\,\mathrm{MHz}$ and $3\,\mathrm{GHz}$ in steps of $3\,\mathrm{MHz}$, using a 201×201 grid with grid-point spacing $1\,\mathrm{mm}$. For the reconstruction algorithm, a 101×101 grid with grid-point spacing $2\,\mathrm{mm}$ was used to avoid "inverse crime". The center frequency and Full-width-at-half-max bandwidth (FWHM bandwidth) for the pulsed signal were here $1.5\,\mathrm{GHz}$ and $0.6\,\mathrm{GHz}$, respectively, corresponding to 401 frequency points. 20 iterations were used in the inverse solver. The produced Debye coefficients were used to calculate a result for $1.5\,\mathrm{GHz}$.

It was concluded that both algorithms produced qualitatively similar images. The FEM code had a shorter reconstruction time, 8 minutes compared to 15 on a regular desktop computer. It also needs frequency data as input.

There is a misprint in the caption of Figure 4 and Figure 5. The captions refer to "Phantom C". In this final version of the paper, only one phantom is studied and there is thus no need to name it.

In this paper, only numerical data is presented. For the conference we had had time to prepare a study on experimental data, for which the reconstructions are presented in Chapter 3.3.1 of the thesis.

4.3   Paper C

In this paper, the hypothesis laid out in Paper A is further studied. It is investigated whether the plastic of the phantom is affecting the images or

not.

The two shells of the phantom are studied one at a time to investigate each shell's contribution to possible image impacts. For each shell, two measurement series are performed. First the shell is filled with the same liquid as in the previous study, i.e. a glycerin-water mixture of ratio 88:12 for the adipose region and 72:28 for the fibroglandular. Second the shells are filled with the same 80:20 mixture as the surrounding coupling bath.

Before the reconstructed images are studied themselves, the raw data is interrogated. This was done to ensure that any anomalies in the images is not just a cause of unknown flaws in the algorithm. Figure 7 shows the raw data obtained from measurements on the inner shell for the two measurements series. The two series produce similar data and it is apparent that the plastic alone could potentially produce an image. In Figure 8, the corresponding interrogation of the outer shell is presented. Also here, the affect of the plastic on the raw data is evident, but it is much less apparent compared to the inner shell.

Following this, the reconstructed images of the two shells are presented. For the outer shell, presented in Figure 12, it is clear that the phantom does appear in the images for imaging planes close to the nipple where the plastic takes up a significant part of the imaging zone. Though, in the 80:20-mixture images, it is much less apparent than in the 88:12 images. For planes further away from the nipple, the affects of the plastic is much less evident in the 80:20 images.

On the other hand, the images of the inner shell presented in Figure 13 show no significant difference between the 80:20 and 72:28 solutions. The phantom is clearly apparent in all of the images and it is not possible to distinguish between the two series. This comes from the fact that this inner shell has a "wrinkled" shape which gives it a larger effective thickness and thus makes it a larger part of the imaging zone.

It is concluded that the large amount of plastic does have a significant impact on the reconstructed images. It is suggested that different materials with properties closer to those of breast tissue be considered for future phantoms.

Chapter 5

Discussion

In this chapter, the major conclusions of the project are summarized. Some suggestions for future work are also stated. These suggestions include continued studies as well as problems that need to be overcome.

5.1 Conclusion

The tomographic system utilized in this project has proved that it is capable of microwave imaging. Images of a simplistic phantom were produced that coincided with the true phantom to a high extent. No *a priori* information about the phantoms was needed or used to produce the images presented in this thesis. The system has also been used to reconstruct images of the GeePs-L2S-breast phantom developed at the Supelec institute, also without the use of *a priori* information.

The GeePs-L2S phantom is an intricate piece that geometrically resembles a human breast to a high extent. Its two hollow shells allow for great versatility when considering different liquids for tissue mimicking purposes such that different property distributions may easily be investigated.

The outer shell of the phantom is regularly shaped and is about 2 mm thin. The inner shape is, on the other hand, mostly irregularly shaped in a "wrinkled" way. This means that the effective thickness of the inner shape is quite large.

Measurements of the phantom using the system described in this thesis have shown that its interior is fairly difficult to reconstruct, although the exterior was well represented in the reconstructed images. A hypothesis was presented that this significant suppression of the interior features were due to the high plastic content of the inner shell.

Further studies of the GeePs-L2S phantom showed that the plastic of especially the inner shell had a sufficient effect on the measurements to produce images on its own. It was therefore concluded that the high plastic content may have significant negative effects on the reconstructions.

An initial comparison between two different reconstruction algorithms has been conducted. One algorithm is a frequency-domain based FEM code and the other is an FDTD algorithm. This initial study has only produced a qualitative comparison between the two codes.

Both algorithms were found to produce images of the interrogated phantom that resembled the phantom well, both in geometry and dielectric properties. The reconstruction times are comparable for the two algorithms but the data acquisition time for the FDTD algorithm is much longer since it demands measurements at many more frequencies. An alternative could be to also perform the measurements in the time domain.

5.2   Future work

The investigation of the GeePs-L2S phantom showed potential problems with reconstructing its interior due to the high plastic content. There are several possible ways to work around this.

The best thing would most likely be to use another kind of material with properties closer to those of breast tissue. Example of this could be the rubber-carbon mixture suggested by Santorelli *et al.* [78] or the conductive plastic suggested by Faenger *et al.* [79] A disadvantage of this could be that it is hard to 3D print.

It could also be argued that a phantom does not have to be as detailed as the GeePs-L2S phantom. Microwaves have a relatively long wave length compared to a human breast and will thus not capture all details present in the studied phantom. It could be made more simplicticly, keeping the general shapes but minimizing many details in order to reduce the amount of plastic and its effective thickness. Another idea would be to use it as a mold for gel based phantoms instead of using it as is.

Finally, the negative effects could be reduced by data processing. For example, a measurement of the phantom filled with the coupling medium could potentially be used as a reference to calibrate the system. These kinds of processing would however add extra steps not necessary in a screening of an actual breast.

It should however be emphasized that this interrogation of the phantom was conducted with one particular system. It would be of great interest to see similar investigations of the plastic's impact on the images conducted on other systems.

For the continued comparison of the two algorithms studied, a more quantitative result is of interest. By using well defined phantoms, it should be measured how much each reconstruction deviates from ground truth, both in terms of permittivity and conductivity. Furthermore, it should be studied if the data acquisition time for the FDTD algorithm can be reduced by

lowering the number of frequency points without reducing the image quality. Finally, it is of interest to further optimize the VNA settings to see whether the image quality can be improved or if higher frequencies can be used.

Bibliography

[1] G. Abdoli, M. Bottai, K. Sandelin, and T. Moradi, "Breast cancer diagnosis and mortality by tumor stage and migration background in a nationwide cohort study in Sweden," *The Breast*, vol. 31, pp. 57 – 65, 2017.

[2] Statistiska centralbyrån. Befolkningsutveckling; födda, döda, in- och utvandring, gifta, skilda 1749–2017. Statistiska centralbyrån. [Online]. Available: http://www.scb.se [Accessed: Aug. 15, 2018].

[3] R. L. Siegel, K. D. Miller, and A. Jemal, "Cancer statistics, 2018," *CA-CANCER J.*, vol. 68, p. 7–30, 2018.

[4] M. Säbel and H. Aichinger, "Recent developments in breast imaging," *Phys. Med. Biol.*, vol. 41, pp. 315–368, 1996.

[5] National Breast Cancer Foundation. Biopsy. National Breast Cancer Foundation. [Online]. Available: http://www.nationalbreastcancer.org [Accessed: Sep. 11, 2018].

[6] Breastcancer.org. CT (CAT) Scans (Computerized Tomography). BreastCancer.org. [Online]. Available: http://www.breastcancer.org/symptoms/testing/types/cat_scans [Accessed: Aug. 23, 2018].

[7] American Cancer Society. Breast MRI Scans. American Cancer Society. [Online]. Available: http://www.cancer.org [Accessed: Aug. 23, 2018].

[8] Breastcancer.org. PET Scans. BreastCancer.org. [Online]. Available: http://www.breastcancer.org/symptoms/testing/types/pet [Accessed: Aug. 23, 2018].

[9] European Medicines Agency, "EMA's final opinion confirms restrictions on use of linear gadolinium agents in body scans," European Medicines Agency, Tech. Rep. EMA/625317/2017, 2017.

[10] National Breast Cancer Foundation. Ultrasound. National Breast Cancer Foundation. [Online]. Available: http://www.nationalbreastcancer.org [Accessed: Aug. 23, 2018].

[11] Breastcancer.org. Digital Tomosynthesis. BreastCancer.org. [Online]. Available: http://www.breastcancer.org/symptoms/testing/types/dig_tomosynth [Accessed: Aug. 23, 2018].

[12] S. Y. Semenov, "Microwave tomography: review of the progress towards clinical applications," *Philos. T. Roy. Soc. A*, vol. 367, pp. 367, 3021, 2009.

[13] M. Persson, A. Fhager, H. D. Trefna, Y. Yu, T. McKelvey, G. Pegenius, J.-E. Karlsson, and M. Elam, "Microwave-based stroke diagnosis making global prehospital thrombolytic treatment possible,," *IEEE Trans. Biomed. Eng.*, vol. 61, pp. 2806–2817, 2014.

[14] J. Ljungqvist, S. Candefjord, M. Persson, L. Jönsson, T. Skoglund, and M. Elam, "Clinical evaluation of a microwave-based device for detection of traumatic intracranial hemorrhage," *J. Neurotraum.*, vol. 34, pp. 2176–2182, 2017.

[15] S. Y. Semenov and D. R. Corfield, "Microwave tomography for brain imaging: Feasibility assessment for stroke detection," *Int. J. Antenn. Propag.*, vol. 2008, p. no. 254830, 2008.

[16] S. Y. Semenov, A. E. Bulyshev, V. G. Posukh, Y. E. Sizov, T. C. Williams, and A. E. Souvorov, "Microwave tomography for detection/imaging of myocardial infarction. i. excised canine hearts," *Ann. Biomed. Eng.*, vol. 31, pp. 262–270, 2003.

[17] P. M. Meaney, D. Goodwin, A. H. Golnabi, T. Zhou, M. Pallone, S. D. Geimer, G. Burke, and K. D. Paulsen, "Clinical microwave tomographic imaging of the calcaneus: A first-in-human case study of two subjects," *IEEE Trans. Biomed. Eng.*, vol. 59, pp. 3304–3313, 2012.

[18] G. Gennarelli, G. Vivone, P. Braca, F. Soldovieri, and M. G. Amin, "Multiple extended target tracking for through-wall radars," *IEEE Trans. Geosci. Remote Sens.*, vol. 53, pp. 6482– 6494, 2015.

[19] L. E. Larsen and J. H. Jacobi, "Microwave scattering parameter imagery of an isolated canine kidney," *Med. Phys.*, vol. 6, pp. 394–403, 1979.

[20] J. Bolomey, A. Izadnegahdar, L. Jofre, C. Pichot, G. Peronnet, and M. Solaimani, "Microwave diffraction tomography for biomedical applications," *IEEE Trans. Microw. Theory Techn.*, vol. 30, p. 1998 –2000, 1982.

[21] C. Pichot, L. Jofre, G. Peronnet, and J. Bolomey, "Active microwave imaging of inhomogeneous bodies," *IEEE Trans. Antennas and Prop.*, vol. 33, pp. 416–425, 1985.

[22] M. Slaney, A. C. Kak, and L. E. Larsen, "Limitations of imaging with first-order diffraction tomography," *IEEE Trans. Microw. Theory Techn.*, vol. 32, no. 8, pp. 860–874, 1984.

[23] P. M. Meaney, A. H. Golnabi, N. R. Epstein, S. D. Geimer, M. W. Fanning, J. B. Weaver, and K. D. Paulsen, "Integration of microwave tomography with magnetic resonance for improved breast imaging," *Med. Phys.*, vol. 40, paper #103101, 2013.

[24] M. Asefi, A. Zakaria, and J. LoVetri, "Microwave imaging using normal electric-field components inside metallic resonant chambers," *IEEE Trans. Microw. Theory Techn.*, vol. 65, no. 3, pp. 923–933, 2017.

[25] K. Nemez, A. Baran, M. Asefi, and J. LoVetri, "Modeling error and calibration techniques for a faceted metallic chamber for magnetic field microwave imaging," *IEEE Trans. Microw Theory Techn.*, vol. 65, no. 11, pp. 4347–4356, 2017.

[26] A. Fhager, S. K. Padhi, and J. Howard, "3D image reconstruction in microwave tomography using an efficient FDTD model," *IEEE Antennas and Wireless Propagation Letters*, vol. 8, pp. 1353–1356, 2009.

[27] R. Scapaticci, I. Catapano, and L. Crocco, "Wavelet-based adaptive multiresolution inversion for quantitative microwave imaging of breast tissue," *IEEE Trans. Antennas Propag.*, vol. 60, pp. 3717–3726, 2012.

[28] J. D. Shea, P. Kosmas, S. C. Hagness, and B. D. van Veen, "Three-dimensional microwave imaging of realistic numerical breast phantoms via a multiple-frequency inverse scattering technique," *Med. Phys.*, vol. 37, pp. 4210–4226, 2010.

[29] A. Fhager, "Microwave tomography," Ph.D. dissertation, Chalmers University of Technology, 2006.

[30] M. Hopfer, R. Planas, A. Hamidipour, T. Henriksson, and S. Semenov, "Electromagnetic tomography for detection, differentiation, and monitoring of brain stroke: A virtual data and human head phantom study." *IEEE Antennas and Propagation Magazine*, vol. 59, no. 5, pp. 86–97, 2017.

[31] M. Klemm, I. J. Craddock, J. A. Leendertz, A. Preece, and R. Benjamin, "Radar-based breast cancer detection using a hemispherical antenna array—experimental results," *IEEE Trans. Antennas and Prop.*, vol. 57, pp. 1692–1704, 2009.

[32] E. C. Fear, J. Bourqui, C. Curtis, D. Mew, B. Docktor, and C. Romano, "Microwave breast imaging with a monostatic radar-based system: a

study of application to patients," *IEEE Trans. Microw. Theory Techn.*, vol. 61, pp. 2119–2128, 2013.

[33] A. W. Preece, I. Craddock, M. Shere, L. Jones, and H. L. Winton, "MARIA M4: Clinical evaluation of a prototype ultrawideband radar scanner for breast cancer detection," *J. Med. Imag.*, vol. 3, paper #033502, 2016.

[34] M. Klemm, J. A. Leendertz, D. Gibbins, I. J. Craddock, A. Preece, and R. Benjamin, "Microwave radar-based breast cancer detection: Imaging in inhomogeneous breast phantoms," *IEEE Antennas Wireless Propag. Lett.*, vol. 8, pp. 1349–1352, 2009.

[35] M. Klemm, I. J. Craddock, A. Preece, J. Leendertz, and R. Benjamin, "Evaluation of a hemi-spherical wideband antenna array for breast cancer imaging," *Radio Sci.*, vol. 43, paper RS6S06, 2008.

[36] E. Porter, M. Coates, and M. Popovic, "An early clinical study of time-domain microwave radar for breast health monitoring," *IEEE Trans. Biomed. Eng.*, vol. 63, pp. 530–539, 2016.

[37] A. Fasoula, L. Duchesne, J. D. G. Cano, P. Lawrence, G. Robin, and J.-G. Bernard, "On-site validation of a microwave breast imaging system, before first patient study," *Diagnostics*, vol. 8, paper #53, 2018.

[38] R. K. Amineh, A. Khalatpour, and N. K. Nikolova, "Three-dimensional microwave holographic imaging using co- and cross-polarized data," *IEEE Trans. Antennas Propag.*, vol. 60, pp. 3526–3531, 2012.

[39] D. M. Sheen, D. L. McMakin, and T. E. Hall, "Three-dimensional millimeter-wave imaging for concealed weapon detection," *IEEE Trans. Microw. Theory Techn.*, vol. 49, pp. 1581–1592, 2001.

[40] P. M. Meaney, M. W. Fanning, D. Li, S. P. Poplack, and K. D. Paulsen, "A clinical prototype for active microwave imaging of the breast," *IEEE Trans. Microw. Theory Techn.*, vol. 48, no. 11, pp. 1841–1853, 2000.

[41] S. P. Poplack, T. D. Tosteson, W. A. Wells, B. W. Pogue, P. M. Meaney, A. Hartov, C. A. Kogel, S. K. Soho, J. J. Gibson, and K. D. Paulsen, "Electromagnetic breast imaging: Results of a pilot study in women with abnormal mammograms," *Radiology*, vol. 243, pp. 350–359, 2007.

[42] P. M. Meaney, M. W. Fanning, T. Raynolds, C. J. Fox, Q. Fang, C. A. Kogel, S. P. Poplack, and K. D. Paulsen, "Initial clinical experience with microwave breast imaging in women with normal mammography," *Acad. Radiol.*, vol. 14, pp. 207–218, 2007.

[43] P. M. Meaney, P. A. Kaufman, L. S. Muffly, M. Click, S. P. Poplack, W. A. Wells, G. N. Schwartz, R. M. di Florio-Alexander, T. D. Tosteson, Z. Li, S. D. Geimer, M. W. Fanning, T. Zhou, N. R. Epstein, and K. D. Paulsen, "Microwave imaging for neoadjuvant chemotherapy monitoring: Initial clinical experience," *Breast Cancer Res.*, vol. 15, paper #35, 2013.

[44] P. Debye, *Polar Molecules.* New York, NY: Chemical Catalog Company, 1929.

[45] K. S. Cole and R. H. Cole, "Dispersion and absorption in dielectrics I. alternating current characteristics," *J Chem. Phys.*, vol. 9, pp. 341–351, 1941.

[46] S. Gabriel, R. W. Lau, and C. Gabriel, "The dielectric properties of biological tissues: III. parametric models for the dielectric spectrum of tissues," *Phys. Med. Biol.*, vol. 41, p. 2271–2293, 1996.

[47] H. Fricke and S. Morse, "The electric capacity of tumors of the breast," *J. Cancer Res.*, vol. 10, no. 3, pp. 340–376, 1926.

[48] H. Q. Woodard and D. R. White, "The composition of body tissues," *Brit. J. Radiol.*, vol. 59, pp. 1209–1219, 1986.

[49] S. Gabriel, R. W. Lau, and C. Gabriel, "The dielectric properties of biological tissues: II. measurements in the frequency range 10 Hz to 20 GHz," *Phys. Med. Biol.*, vol. 41, pp. 2251–2269, 1996.

[50] M. Lazebnik, D. Popovic, L. McCartney, C. B. Watkins, M. J. Lindstrom, J. Harter, S. Sewall, T. Ogilvie, A. Magliocco, T. M. Breslin, W. Temple, D. Mew, J. H. Booske, M. Okoniewski, and S. C. Hagness, "A large-scale study of the ultrawideband microwave dielectric properties of normal, benign and malignant breast tissues obtained from cancer surgeries," *Phys. Med. Biol.*, vol. 52, pp. 6093–6115, 2007.

[51] T. Sugitani, S.-i. Kubota, S.-i. Kuroki, K. Sogo, K. Arihiro, M. Okada, T. Kadoya, M. Hide, M. Oda, and T. Kikkawa, "Complex permittivities of breast tumor tissues obtained from cancer surgeries," *Appl. Phys. Lett.*, vol. 104, paper #253702, 2014.

[52] T. Sugitani, S.-i. Kubota, S.-i. Kuroki, K. Sogo, K. Arihiro, M. Okada, T. Kadoya, M. Hide, M. Oda, and T. Kikkawa, "Erratum: "complex permittivities of breast tumor tissues obtained from cancer surgeries" [appl. phys. lett. 104, 253702 (2014)]," *Appl. Phys. Lett.*, vol. 107, paper #019902, 2015.

[53] A. Martellosio, M. Pasian, M. Bozzi, L. Perregrini, A. Mazzanti, F. Svelto, P. E. Summers, G. Renne, L. Preda, and M. Bellomi, "Dielectric properties characterization from 0.5 to 50 GHz of breast cancer tissues," *IEEE Trans. Microw. Theory Techn.*, vol. 65, pp. 998–1011, 2017.

[54] Y. Cheng and M. Fu, "Dielectric properties for non-invasive detection of normal, benign, and malignant breast tissues using microwave theories," *Thoracic Cancer*, vol. 9, pp. 459–465, 2018.

[55] S. Salah-Ud-Din, P. M. Meaney, E. Porter, and M. O'Halloran, "Investigation of abscissa scales for dielectric measurements of biological tissues," *Biomed. Phys. Eng. Express*, vol. 3, paper #015020, 2017.

[56] P. M. Meaney, A. Gregory, N. Epstein, and K. D. Paulsen, "Microwave open-ended coaxial dielectric probe: interpretation of the sensing volume re-visited," *BMC Med. Phys.*, vol. 14, paper #1756-6649, 2014.

[57] P. M. Meaney, A. P. Gregory, J. Seppälä, and T. Lahtinen, "Open-ended coaxial dielectric probe effective penetration depth determination," *IEEE Trans. Microw. Theory Techn.*, vol. 64, pp. 915–923, 2016.

[58] O. Casas, R. Bragos, P. Riu, J. Rosell, M. Tresanchez, M. Warren, A. Rodriguez-Sinovas, A. Carreno, and J. Cinca, "In vivo and in situ ischemic tissue characterization using electrical impedance spectroscopy," *Ann. NY Acad. Sci.*, vol. 873, pp. 51–58, 1999.

[59] D. Haemmerich, O. R. Ozkan, J. Z. Tsai, S. T. Staelin, S. Tungjitkusolmun, D. M. Mahvi, and J. G. Webster, "Changes in electrical resistivity of swine liver after occlusion and postmortem," *Med. Biol. Eng. Comput.*, vol. 40, pp. 29–33, 2002.

[60] D. M. Pozar, *Microwave Engineering*, 4th ed. Hoboken, NJ: John Wiley & Sons, Inc., 2011.

[61] G. T. Herman, *Fundamentals of computerized tomography: Image reconstruction from projection*, 2nd ed. London, UK: Springer, 2009.

[62] P. M. Meaney, N. K. Yagnamurthy, and K. D. Paulsen, "Pre-scaled two-parameter Gauss-Newton image reconstruction to reduce property recovery imbalance," *Phys. Med. Biol.*, vol. 47, pp. 1101–1119, 2002.

[63] P. M. Meaney, S. D. Geimer, and K. D. Paulsen, "Two-step inversion in microwave imaging with a logarithmic transformation," *Med. Phys.*, vol. 44, pp. 4239–4251, 2017.

[64] P. M. Meaney, K. D. Paulsen, B. W. Pogue, and M. I. Miga, "Microwave image reconstruction utilizing log-magnitude and unwrapped

phase to improve high-contrast object recovery," *IEEE Trans. Med. Imag.*, vol. 20, pp. 104–116, 2001.

[65] P. M. Meaney, Q. Fang, T. Rubaek, E. Demidenko, and K. D. Paulsen, "Log transformation benefits parameter estimation in microwave tomographic imaging," *Med. Phys.*, vol. 34, pp. 2014–2023, 2007.

[66] P. Hashemzadeh, A. Fhager, and M. Persson, "Experimental investigation of an optimization approach to microwave tomography," *Electromagn. Biol. Med.*, vol. 25, pp. 1–12, 2006.

[67] A. Fhager, M. Gustafsson, and S. Nordebo, "Image reconstruction in microwave tomography using a dielectric debye model," *IEEE Trans. Biomed. Eng.*, vol. 59, pp. 156–166, 2012.

[68] A. Fhager, P. Hashemzadeh, and M. Persson, "Reconstruction quality and spectral content of an electromagnetic time-domain inversion algorithm," *IEEE Trans. Biomed. Eng.*, vol. 53, no. 8, pp. 1594 – 1604, 2006.

[69] N. Joachimowicz, C. Conessa, T. Henriksson, and B. Duchêne, "Breast phantoms for microwave imaging," *IEEE Antennas Wireless Propag. Lett.*, vol. 13, pp. 1333–1336, 2014.

[70] P. M. Meaney, C. J. Fox, S. D. Geimer, and K. D. Paulsen, "Electrical characterization of glycerin:water mixtures and the implications for use as a coupling medium in microwave tomography," *IEEE Trans. Microw. Theory Techn.*, vol. 65, pp. 1471–1478, 2017.

[71] M. Habibi, D. P. Klemer, and V. Raicu, "Two-dimensional dielectric spectroscopy: Implementation and validation of a scanning open-ended coaxial probe," *Rev. Sci. Instrum.*, vol. 81, paper #075108, 2010.

[72] N. Joachimowicz, B. Duchêne, C. Conessa, and O. Meyer, "Reference phantoms for microwave imaging," in *In Proceedings of the 11th European Conference on Antennas and Propagation (EuCAP)*, Paris, France, 2017.

[73] M. Koutsoupidou, I. S. Karanasiou, C. G. Kakoyiannis, E. Groumpas, C. Conessa, N. Joachimowicz, and B. Duchêne, "Evaluation of a tumor detection microwave system with a realistic breast phantom," *Microw. Opt. Techn. Lett.*, vol. 59, pp. 6–10, 2016.

[74] Z. Miao, S. Ahsan, P. Kosmas, J. A. Tobon Vasquez, F. Vipiana, M. R. Casu, and M. Vacca, "Application of the DBIM-TwIST algorithm to experimental microwave imaging data," in *In Proceedings of the 11th European Conference on Antennas and Propagation (EuCAP)*, Paris, France, 2017.

[75] J. A. Tobon Vasquez, F. Vipiana, M. R. Casu, M. Vacca, I. Sarwar, R. Scapaticci, N. Joachimowicz, and B. Duchêne, "Experimental assessment of qualitative microwave imaging using a 3-D realistic breast phantom," in *In Proceedings of the 11th European Conference on Antennas and Propagation (EuCAP)*, Paris, France, 2017.

[76] M. R. Casu, M. Vacca, J. A. Tobon, A. Pulimeno, I. Sarwar, R. Solimente, and F. Vipiana, "A COTS-based microwave imaging system for breast-cancer detection," *IEEE Trans. Microw. Theory Techn.*, vol. 11, pp. 804–814, 2017.

[77] D. R. Herrera, T. Reimer, M. S. Nepote, and S. Pistorius, "Manufacture and testing of anthropomorphic 3D-printed breast phantoms using a microwave radar algorithm optimized for propagation speed," in *In Proceedings of the 11th European Conference on Antennas and Propagation (EuCAP)*, Paris, France, 2017.

[78] A. Santorelli, O. Laforest, E. Porter, and M. Popović, "Image classification for a time-domain microwave radar system: Experiments with stable modular breast phantoms," in *In Proceedings of the 9th European Conference on Antennas and Propagation (EuCAP)*, Lisbon, Portugal, 2015.

[79] B. Faenger, S. Ley, M. Helbig, J. Sachs, and I. Hilger, "Breast phantom with a conductive skin layer and conductive 3D-printed anatomical structures for microwave imaging," in *In Proceedings of the 11th European Conference on Antennas and Propagation (EuCAP)*, Paris, France, 2017.

[80] M. J. Burfeindt, T. J. Colgan, R. O. Mays, J. D. Shea, N. Behdad, B. D. V. Veen, and S. C. Hagness, "Mri-derived 3-d-printed breast phantom for microwave breast imaging validation," *IEEE Antennas Wireless Propag. Lett.*, vol. 11, pp. 1610–1613, 2012.

[81] N. R. Epstein, P. M. Meaney, and K. D. Paulsen, "3d parallel-detection microwave tomography for clinical breast imaging," *Rev. Sci. Instrum.*, vol. 85, p. Art. no. 124704, 2014.

[82] N. Joachimowicz, B. Duchêne, C. Conessa, and O. Meyer, "Easy-to-produce adjustable realistic breast phantoms for microwave imaging," in *In Proceedings of the 10th European Conference on Antennas and Propagation (EuCAP)*, Davos, Switzerland, 2016.

[83] J. E. Joy, E. E. Penhoet, and D. B. Petitti, Eds., *Saving Women's Lives: Strategies for Improving Breast Cancer Detection and Diagnosis.* Washington, DC: The National Academies Press, 2005.

[84] M. Lazebnik, E. Madsen, G. R. Frank, and S. C. Hagness, "Tissue-mimicking phantom materials for narrowband and ultrawideband microwave applications," *Phys. Med. Biol.*, vol. 50, pp. 4245–4258, 2005.

[85] K. Levenberg, "A method for the solution of certain non-linear problems in least squares," *Q. Appl. Math.*, vol. 2, pp. 164–168, 1944.

[86] D. Marquardt, "An algorithm for least-squares estimation of nonlinear parameters," *SIAM J. Appl. Math.*, vol. 211, pp. 431–441, 1963.

[87] P. M. Meaney, F. Schubitidze, M. W. Fanning, M. Kmiec, N. Epstein, and K. D. Paulsen, "Surface-wave multipath signals in near-field microwave imaging," *Int. J. Biomed. Imag.*, vol. 2012, paper #697253, 2012.

[88] U. of Wisconsin Cross-Disciplinary Electromagnetics Laboratory. Phantom repository. University of Wisconsin. [Online]. Available: http://uwcem.ece.wisc.edu/phantomRepository.html [Accessed: Jul. 3, 2017].

[89] Rohde & Schwarz GmbH & Co. KG, "R&S ZNBT8 Vector Network Analyzer Specifications," 2015.

[90] ——, "R&S ZNB/ZNBT Vector Network Analyzers User Manual," 2015.

[91] T. Rubæk, P. M. Meaney, P. Meincke, and P. K. D., "Nonlinear microwave imaging for breast-cancer screening using gauss–newton's method and the cgls inversion algorithm," *IEEE Trans. Antennas Propag.*, vol. 55, pp. 2320–2331, 2017.

[92] T. Rydholm, A. Fhager, M. Persson, and P. M. Meaney, "A first evaluation of the realistic supelec-breast phantom," *IEEE J-ERM*, vol. 1, pp. 59–65, 2017.

[93] T. Rydholm, A. Fhager, M. Persson, S. D. Geimer, and P. M. Meaney, "Effects of the plastic of the realistic geeps-l2s-breast phantom," *Diagnostics*, vol. 8, no. 3, p. #61, 2018.